OPEN ACCESS



The Circumstellar Environments of Double-peaked, Calcium-strong Transients 2021gno and 2021inl

```
W. V. Jacobson-Galán<sup>1</sup>, P. Venkatraman<sup>1</sup>, R. Margutti<sup>1</sup>, D. Khatami<sup>2</sup>, G. Terreran<sup>3</sup>, R. J. Foley<sup>4</sup>, R. Angulo<sup>4</sup>, C. R. Angus<sup>5</sup>, K. Auchettl<sup>4,6,7</sup>, P. K. Blanchard<sup>8</sup>, A. Bobrick<sup>9</sup>, J. S. Bright<sup>1</sup>, D. Brout<sup>10</sup>, K. C. Chambers<sup>11</sup>, C. D. Couch<sup>4</sup>, D. A. Coulter<sup>4</sup>, K. Clever<sup>4</sup>, K. W. Davis<sup>4</sup>, T. J. L. de Boer<sup>11</sup>, L. DeMarchi<sup>8</sup>, S. A. Dodd<sup>4,20</sup>, D. O. Jones<sup>4</sup>,
J. Johnson<sup>4</sup>, C. D. Kilpatrick<sup>8</sup>, N. Khetan<sup>5</sup>, Z. Lai<sup>4</sup>, D. Langeroodi<sup>5</sup>, C.-C. Lin<sup>11</sup>, E. A. Magnier<sup>11</sup>, D. Milisavljevic<sup>12</sup>, H. B. Perets<sup>9</sup>, J. D. R. Pierel<sup>13</sup>, J. Raymond<sup>10</sup>, S. Rest<sup>14</sup>, A. Rest<sup>12,14</sup>, R. Ridden-Harper<sup>15</sup>, K. J. Shen<sup>2</sup>, M. R. Siebert<sup>4</sup>, C. Smith<sup>4</sup>, K. Taggart<sup>4</sup>, S. Tinyanont<sup>4</sup>, F. Valdes<sup>16</sup>, V. A. Villar<sup>17,18,19</sup>, Q. Wang<sup>14</sup>,
                                                                     S. K. Yadavalli<sup>17</sup>, Y. Zenati<sup>14</sup>, and A. Zenteno<sup>16</sup>
                              Department of Astronomy and Astrophysics, University of California, Berkeley, CA 94720, USA; wynnjg@berkeley.edu
                                    Department of Astronomy and Theoretical Astrophysics Center, University of California, Berkeley, CA 94720, USA
                                                        Las Cumbres Observatory, 6740 Cortona Drive, Suite 102, Goleta, CA 93117-5575, USA
                                              <sup>4</sup> Department of Astronomy and Astrophysics, University of California, Santa Cruz, CA 95064, USA
                                            DARK, Niels Bohr Institute, University of Copenhagen, Jagtvej 128, DK-2200 Copenhagen, Denmark
                                                                     <sup>6</sup> School of Physics, The University of Melbourne, VIC 3010, Australia
                                                  <sup>7</sup> ARC Centre of Excellence for All Sky Astrophysics in 3 Dimensions (ASTRO 3D), Australia
<sup>8</sup> Center for Interdisciplinary Exploration and Research in Astrophysics (CIERA), and Department of Physics and Astronomy, Northwestern University, Evanston, IL
                                                                                                                 60208, USA
                                                         <sup>9</sup> Technion—Israel Institute of Technology, Physics department, Haifa 3200002, Israel
                                               Center for Astrophysics Harvard & Smithsonian, 60 Garden Street, Cambridge, MA 02138, USA
                                               <sup>11</sup> Institute for Astronomy, University of Hawaii, 2680 Woodlawn Drive, Honolulu, HI 96822, USA
                              Department of Physics and Astronomy, Purdue University, 525 Northwestern Avenue, West Lafayette, IN 47907, USA

13 Space Telescope Science Institute, Baltimore, MD 21218, USA
                                             <sup>14</sup> Department of Physics and Astronomy, The Johns Hopkins University, Baltimore, MD 21218, USA
                15 School of Physical and Chemical Sciences | Te Kura Matū, University of Canterbury, Private Bag 4800, Christchurch 8140, New Zealand
16 Cerro Tololo Inter-American Observatory, NSF's National Optical-Infrared Astronomy Research Laboratory, Casilla 603, La Serena, Chile
17 December 18 Astronomy Research Laboratory, Park PA 16803, USA
                       Department of Astronomy and Astrophysics, Pennsylvania State University, 525 Davey Laboratory, University Park, PA 16802, USA

18 Institute for Computational & Data Sciences, The Pennsylvania State University, University Park, PA, USA
                                     <sup>19</sup> Institute for Gravitation and the Cosmos, The Pennsylvania State University, University Park, PA 16802, USA
                                                   Received 2022 March 3; revised 2022 April 8; accepted 2022 April 8; published 2022 June 15
```

Abstract

We present panchromatic observations and modeling of calcium-strong supernovae (SNe) 2021gno in the star-forming host-galaxy NGC 4165 and 2021inl in the outskirts of elliptical galaxy NGC 4923, both monitored through the Young Supernova Experiment transient survey. The light curves of both, SNe show two peaks, the former peak being derived from shock cooling emission (SCE) and/or shock interaction with circumstellar material (CSM). The primary peak in SN 2021gno is coincident with luminous, rapidly decaying X-ray emission ($L_x = 5 \times 10^{41}$ erg s⁻¹) detected by Swift-XRT at $\delta t = 1$ day after explosion, this observation being the second-ever detection of X-rays from a calcium-strong transient. We interpret the X-ray emission in the context of shock interaction with CSM that extends to $r < 3 \times 10^{14}$ cm. Based on X-ray modeling, we calculate a CSM mass $M_{\rm CSM} = (0.3-1.6) \times 10^{-3}~M_{\odot}$ and density $n = (1-4) \times 10^{10}~{\rm cm}^{-3}$. Radio nondetections indicate a low-density environment at larger radii ($r > 10^{16}~{\rm cm}$) and mass-loss rate of $\dot{M} < 10^{-4}~M_{\odot}$ yr⁻¹. SCE modeling of both primary light-curve peaks indicates an extended-progenitor envelope mass $M_e = 0.02-0.05~M_{\odot}$ and radius $R_e = 30-230~R_{\odot}$. The explosion properties suggest progenitor systems containing either a low-mass massive star or a white dwarf (WD), the former being unlikely given the lack of local star formation. Furthermore, the environments of both SNe are consistent with low-mass hybrid He/C/O WD + C/O WD mergers.

Unified Astronomy Thesaurus concepts: Supernovae (1668); X-ray transient sources (1852); X-ray telescopes (1825); White dwarf stars (1799)

Supporting material: machine-readable tables, data behind figures

1. Introduction

Calcium-rich (Ca-rich) transients are a peculiar class of stellar explosions whose progenitor system remains ambiguous (Filippenko et al. 2003; Perets et al. 2010; Kasliwal et al.

Original content from this work may be used under the terms of the Creative Commons Attribution 4.0 licence. Any further distribution of this work must maintain attribution to the author(s) and the title of the work, journal citation and DOI.

2012). These SNe are defined primarily based on an observed integrated emission line flux ratio of [Ca II]/[O I] > 2 when the explosion has reached its nebular phase (Milisavljevic et al. 2017) and the current sample consists of $N \gtrsim 25$ confirmed objects. Consequently, these SNe are labeled as "Ca-rich" compared to other transients when observed in their optically thin regime. However, because modeling of these SNe has indicated that they do not in fact produce more Ca in an abundance relative to O (Milisavljevic et al. 2017; Jacobson-Galán et al. 2020a, 2021), but rather are simply "rich" in Ca II emission, we choose to adopt an alternative naming convention

²⁰ NASA Einstein Fellow.

and refer to these as "Ca-strong transients" (CaSTs) from this point forward (Shen et al. 2019).

Beyond their prominent Ca II emission, CaSTs have other observational characteristics that make them a well-defined explosion class. First, these SNe are typically low-luminosity explosions $(M_{\text{peak}} > -16.5 \text{ mag})$ that have fast photometric evolutions (e.g., rise-times $\lesssim 15$ days; Taubenberger 2017). Physically, CaSTs are typically low-energy explosions $(E_k \approx 10^{50} \text{ erg})$ that produce small amounts of ejecta ($\lesssim 0.6 \ M_{\odot}$) and 56 Ni ($\lesssim 0.1 M_{\odot}$); the latter being the dominant radioactive isotope that dictates their peak light-curve luminosities. Spectroscopically, most CaSTs exhibit type I spectra with prominent He I transitions at early times and then experience an expedited transition to nebular phases where [Ca II] dominates. Lastly, the explosion environments of early samples of CaSTs showed a strong preference toward the outskirts of early-type galaxies where no star formation was detected, indicating a compact progenitor star, e.g., a white dwarf (WD) system (Perets et al. 2010, 2011; Kasliwal et al. 2012; Lyman et al. 2014; Foley 2015; Lunnan et al. 2017; Dong et al. 2022). However, as the sample of confirmed CaSTs has grown, there has been an increased diversity in the host environments of new objects. For example, CaSTs such as iPTF15eqv (Milisavljevic et al. 2017), iPTF16hgs (De et al. 2018a), SN 2016hnk (Galbany et al. 2019; Jacobson-Galán et al. 2020b), and SN 2019ehk (Jacobson-Galán et al. 2020a; Nakaoka et al. 2021) were all discovered in star-forming host-galaxies, while a number of CaSTs reported in a recent sample by De et al. (2020) continued to show a preference toward early-type hosts.

Many of these SNe were found at relatively large offsets from their host-galaxy nuclei (Perets & Beniamini 2021, and references therein), showing a different offset distribution than type Ia SNe (Kasliwal et al. 2012), which prompts suggestions of the progenitors residing in globular clusters or ejected at high velocities from their original formation closer to the hostgalaxy nuclei (Perets et al. 2010; Foley 2015; Shen et al. 2019). However, a more detailed study (Perets & Beniamini 2021) showed that the large offsets originate from the SNe in earlytype galaxies (also consistent with the two new SNe that we discuss here), where a large fraction of the CaST SNe are found. In such galaxies, the old stellar population extends to large distances, and the overall large offset distribution is consistent with the distribution of the old stellar populations in such galaxies, further supporting old stellar progenitors for likely the majority of the CaST SNe (Perets 2014; Perets & Beniamini 2021).

While the heterogeneous environments of CaSTs make it difficult to constrain a single progenitor channel, there have been significant constraints made to the parameter space of viable CaST progenitor systems. First, the discovery of multiple CaSTs with double-peaked light curves (e.g., iPTF16hgs, SN 2018lqo, SN 2019ehk; De et al. 2018a, 2020; Jacobson-Galán et al. 2020a) has indicated that the progenitors of at least some of these transients must arise from stars surrounded by either extended envelopes or confined circumstellar material (CSM). Another major breakthrough in the study of these objects came from the discovery of the closest CaST to date, SN 2019ehk, which exploded in the spiral host-galaxy M100 at $D \approx 16.2$ Mpc (Jacobson-Galán et al. 2020a; Nakaoka et al. 2021; De et al. 2021). SN 2019ehk was detected within \sim 10 hr of explosion and produced luminous X-ray emission, coincident with shockionized spectral emission lines, and a double-peaked light curve

(Jacobson-Galán et al. 2020a, hereafter WJG20a). The combination of these observations (X-ray to radio) revealed that the SN 2019ehk progenitor star exploded into a confined shell of H-and He-rich CSM with mass of $\sim 7 \times 10^{-3} M_{\odot}$. Furthermore, SN 2019ehk is the first CaST with preexplosion Hubble Space Telescope imaging, which revealed no detectable progenitor, but did constrain the possible progenitor channels to a low-mass massive star ($< 10 M_{\odot}$) or a WD system. Lastly, given its close proximity, SN 2019ehk was imaged out to ~ 400 days post explosion, which allowed for the tightest constraints to date to be made on the total amount of synthesized-radioactive-decay isotopes ⁵⁶Ni and ⁵⁷Ni in a CaST; the isotope mass ratio suggests a progenitor channel involving the merger of low-mass WDs (Jacobson-Galán et al. 2021).

In this paper, we present, analyze, and model multiwavelength observations (X-ray to radio) of two new CaSTs, SNe 2021 gno and 2021inl, both with double-peaked optical light curves. SN 2021gno was discovered with an apparent magnitude of 18.2 mag by the Zwicky Transient Facility (ZTF) on 2021 March 20 (MJD 59293.2) and is located at $\alpha = 12^{h}12^{m}10.29^{s}$, $\delta =$ +13°14′57.04″ (Bruch et al. 2021). While SN 2021gno was originally classified as both a type II and type IIb supernova (SN; Hung et al. 2021), the spectral time series, coupled with its lightcurve evolution, indicates that it belongs in the CaST class. SN 2021inl was discovered by ZTF on 2021 April 07 (MJD 59311.2) with a detection magnitude of 19.5 mag and is located at $\alpha = 13^{\text{h}}01^{\text{m}}33.24^{\text{s}}$, $\delta = +27^{\circ}49'55.10''$ (Munoz-Arancibia et al. 2021). SN 2021inl was classified as a type Ib-peculiar and was noted to be spectroscopically consistent with the "Carich" transient class (Taggart et al. 2021).

SN 2021gno is located 23".3 NW of the nucleus of the SABa galaxy NGC 4165. For SN 2021gno, we use the redshiftindependent distance of 30.5 ± 5.6 Mpc, which was calculated using the Tully-Fisher relation (Theureau et al. 2007). For SN 2021inl, we use a redshift $z = 0.0182 \pm 0.0001$ (Albareti et al. 2017), which corresponds to a distance of 79.9 ± 0.4 Mpc for standard Λ CDM cosmology ($H_0 = 70 \text{ km s}^{-1} \text{ Mpc}^{-1}$, $\Omega_M = 0.27$, $\Omega_{\Lambda} = 0.73$); unfortunately no redshift-independent distance is available. Possible uncertainties on the SN 2021inl distance could be the choice of H_0 and/or peculiar velocities of the host-galaxy; the uncertainty on the former can, for example, contribute to ≤5% uncertainty of the SN luminosity. For each SN, we define the time of explosion as the mean phase between last nondetection and first detection. This results in a time of explosion of MJD 59292.7 \pm 0.6 days (2021 March 19) for SN 2021gno and MJD 59309.4 \pm 0.1 days (2021 April 05) for SN 2021inl. The main parameters of SNe 2021gno and 2021inl and their host-galaxies (Figure 1) are displayed in Tables 1 and 2, respectively.

2. Observations

2.1. UV/Optical/NIR Photometry

SN 2021gno was observed with the Ultraviolet Optical Telescope (UVOT; Roming et al. 2005) on board the Neil Gehrels Swift Observatory (Gehrels et al. 2004) from 2021 March 20 until 2021 April 21 (δ t= 0.84–33.0 days since explosion). We performed aperture photometry with a 5" region with uvotsource within HEAsoft v6.26, 21 following the standard guidelines from Brown et al. (2014). In order to

 $[\]overline{^{21}}$ We used the calibration database (CALDB) version 20201008.

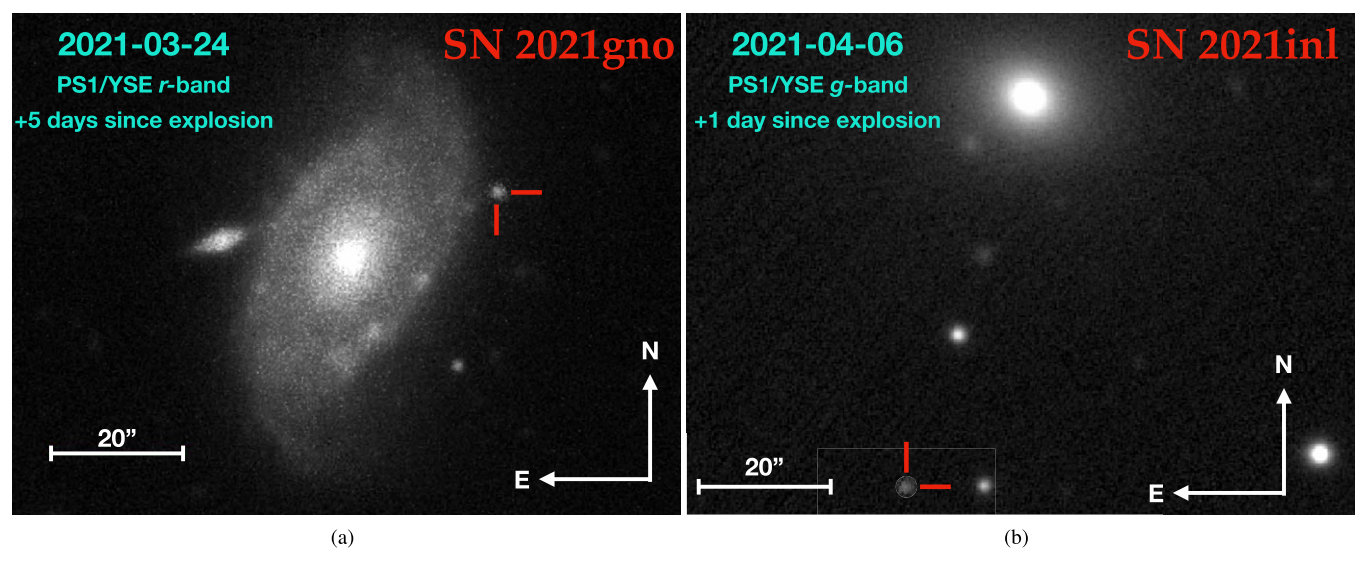


Figure 1. (a) PS1/YSE r-band explosion image of Ca-strong SN 2021gno in host-galaxy NGC 4165. (b) PS1/YSE g-band explosion image of Ca-strong SN 2021inl, offset from host-galaxy NGC 4923 by 60".

Table 1
Main Parameters of SN 2021gno and Its Host-galaxy

Host-galaxy	NGC 4165
Galaxy Type	SAB(r)a
Galactic Offset	24.3"(3.6 kpc)
Redshift	0.0062 ± 0.0002
Distance	$30.5 \pm 5.6 \mathrm{Mpc^a}$
Distance Modulus, μ	$32.4\pm0.4~\mathrm{mag}$
RA_{SN}	$12^{\rm h}12^{\rm m}10.29^{\rm s}$
Dec_{SN}	+13°14′57.04″
Time of Explosion (MJD)	59292.7 ± 0.6
$E(B-V)_{MW}$	$0.030 \pm 0.001 \; \mathrm{mag}$
$E(B-V)_{\text{host}}$	0.0^{b}
$m_g^{ m peak}$	$17.50 \pm 0.03~{ m mag}$
$M_g^{ m peak}$	$-14.9 \pm 0.1~\text{mag}^\text{c-d}$

Notes. No extinction corrections have been applied to the presented apparent magnitudes.

remove contamination from the host-galaxy, we employed images acquired at $t \approx 122$ days after explosion, assuming that the SN contribution is negligible at this phase. This is supported by visual inspection in which we found no flux associated with SN 2021gno. We subtracted the measured count rate at the location of the SN from the count rates in the SN images following the prescriptions of Brown et al. (2014). Consequently, we detect bright UV emission from the SN directly after explosion (Figure 2) until the maximum bolometric light. Subsequent nondetections in w1, m2, w2 bands indicate significant cooling of the photosphere and/or Fe-group line blanketing.

Additional *griz*-band imaging of SN 2021gno and SN 2021inl was obtained through the Young Supernova Experiment (YSE; Jones et al. 2021) with the Pan-STARRS telescope (PS1; Kaiser et al. 2002) between 2021 March 24 and 2021 July 21 ($\delta t = 4.80 - 123.5$ days since explosion) and 2021 April 06 and 2021 June 10 ($\delta t = 0.97 - 66.0$ days since explosion), respectively. PS1

Table 2
Main Parameters of SN 2021inl and Its Host-galaxy

Host-galaxy	NGC 4923
Galaxy Type	E/S0
Galactic Offset	60.0"(23.3 kpc)
Redshift	0.0182 ± 0.0001^{a}
Distance	$79.9 \pm 0.4 \mathrm{Mpc}$
Distance Modulus, μ	$34.50 \pm 0.01 \text{ mag}$
RA_{SN}	13 ^h 01 ^m 33.24 ^s
Dec_{SN}	+27°49′55.10″
Time of Explosion (MJD)	59309.4 ± 0.1
$E(B-V)_{MW}$	$0.008 \pm 0.001 \; \mathrm{mag}$
$E(B-V)_{\text{host}}$	$0.0^{\mathbf{b}}$
m_g^{peak}	$20.2 \pm 0.1~\mathrm{mag}$
$M_g^{ m peak}$	$-14.3\pm0.2~\mathrm{mag}^{\mathrm{c}~\mathrm{d}}$

Notes. No extinction corrections have been applied to the presented apparent magnitudes.

images of SNe 2021gno and 2021inl are presented in Figure 1. Furthermore, SN 2021gno was observed with the DECam Extension survey of YSE between 2021 March 22 and 2022 January 09 ($\delta t = 1.49 - 294.7$ days) on the Cerro Tololo Inter-American Observatory Blanco 4 m telescope (Rest et al. 2022). The YSE photometric pipeline is based on photpipe (Rest et al. 2005). Each image template was taken from stacked PS1 exposures, with most of the input data from the PS1 3π survey. All images and templates are resampled and astrometrically aligned to match a skycell in the PS1 sky tessellation. An image zero-point is determined by comparing point-spread-function (PSF) photometry of the stars to the updated stellar catalogs of PS1 observations (Chambers et al. 2017). The PS1 templates are convolved with a three-Gaussian kernel to match the PSF of the nightly images, and the convolved templates are subtracted from the nightly images with HOTPANTS (Becker 2015). Finally, a flux-weighted centroid is found for each SN position, and PSF photometry is performed using forced photometry: the centroid of

^a Theureau et al. (2007).

^b No host reddening detected at explosion site.

^c Extinction correction applied.

^d Relative to second *g*-band light-curve peak.

^a Albareti et al. (2017).

^b No host reddening detected at explosion site.

^c Extinction correction applied.

d Relative to second g-band light-curve peak.

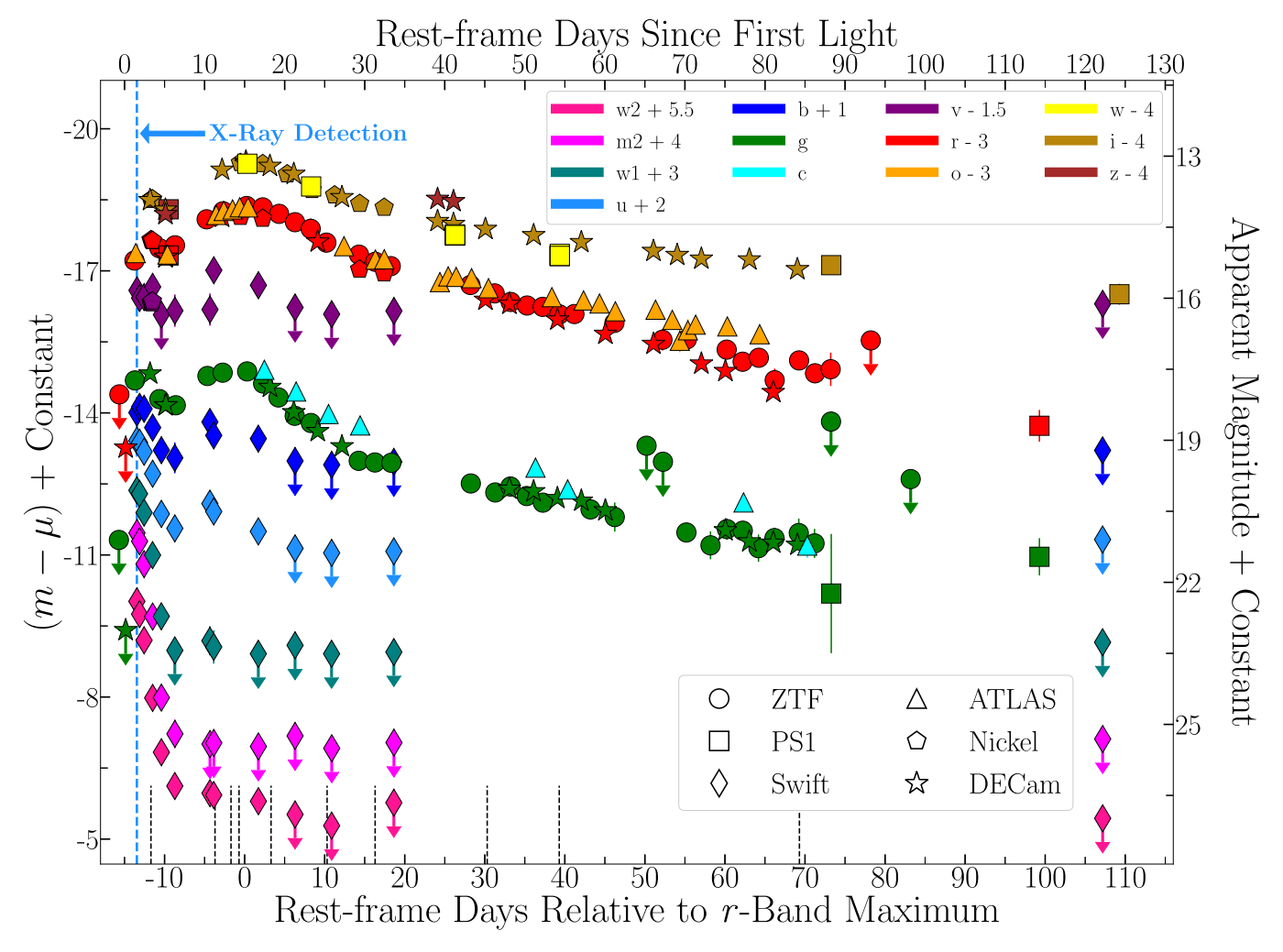


Figure 2. UV/Optical/NIR light curve of SN 2021gno with respect to second r-band maximum ($\delta t \approx 15$ days). Peak of primary light-curve peak occurs at phase $\delta t \approx 2$ days. Observed photometry (absolute and apparent magnitudes) is presented in the AB magnitude system. ATLAS data/ 3σ upper limits are presented as triangles, PS1/YSE as squares, Swift as diamonds, ZTF as circles, Nickel as polygons, and DECam as stars. The epochs of our spectroscopic observations are marked by black dashed lines. Blue vertical dashed line marks the time of the X-ray detection in SN 2021gno.

the PSF is forced to be at the SN position. The nightly zero-point is applied to the photometry to determine the brightness of the SN for that epoch.

Both SNe 2021gno and 2021inl were observed with ATLAS $(\delta t = 0.70 - 84.6$ and $\delta t = 0.10 - 28.1$ days since explosion, respectively), a twin 0.5 m telescope system installed on Haleakala and Mauna Loa in the Hawai'ian islands that robotically surveys the sky in cyan (c) and orange (o) filters (Tonry et al. 2018a). The survey images are processed as described in Tonry et al. (2018a) and photometrically and astrometrically calibrated immediately (using the RefCat2 catalog; Tonry et al. 2018b). Template generation, image subtraction procedures, and identification of transient objects are described in Smith et al. (2020). PSF photometry is carried out on the different images, and all sources greater than 5σ are recorded, and all sources go through an automatic validation process that removes spurious objects (Smith et al. 2020). Photometry on the different images (both forced and nonforced) is from an automated PSF fitting as documented in Tonry et al. (2018a). The photometry presented here is weighted averages of the nightly individual 30 s exposures, carried out with forced photometry at the position of the SNe.

The complete light curves of SNe 2021gno and 2021inl are presented in Figures 2 and 3, respectively, and all photometric observations are listed in Appendix Tables A7 and A8. In addition to our observations, we include g/r-band photometry of SNe 2021gno and 2021inl from the ZTF (Bellm et al. 2019; Graham et al. 2019) forced-photometry service (Masci et al. 2019), which span from 2021 March 20 to 2021 June 15 (δ t=0.54-87.5 days since explosion) and 2021 April 07 to 2021 May 08 (δ t=1.85-32.9 days since explosion).

The Milky Way (MW) V-band extinction and color excess along the SN 2021gno line of sight is $A_V = 0.093$ mag and E(B-V) = 0.03 mag (Schlegel et al. 1998; Schlafly & Finkbeiner 2011), respectively, which we correct for using a standard Fitzpatrick (1999) reddening law ($R_V = 3.1$). Additionally, the MW V-band extinction and color excess along the SN 2021inl line of sight is $A_V = 0.025$ mag and E(B-V) = 0.008 mag (Schlegel et al. 1998; Schlafly & Finkbeiner 2011). For both SNe, we do not correct for host-galaxy contamination given the absence of Na I D absorption in all spectra at the host redshift.

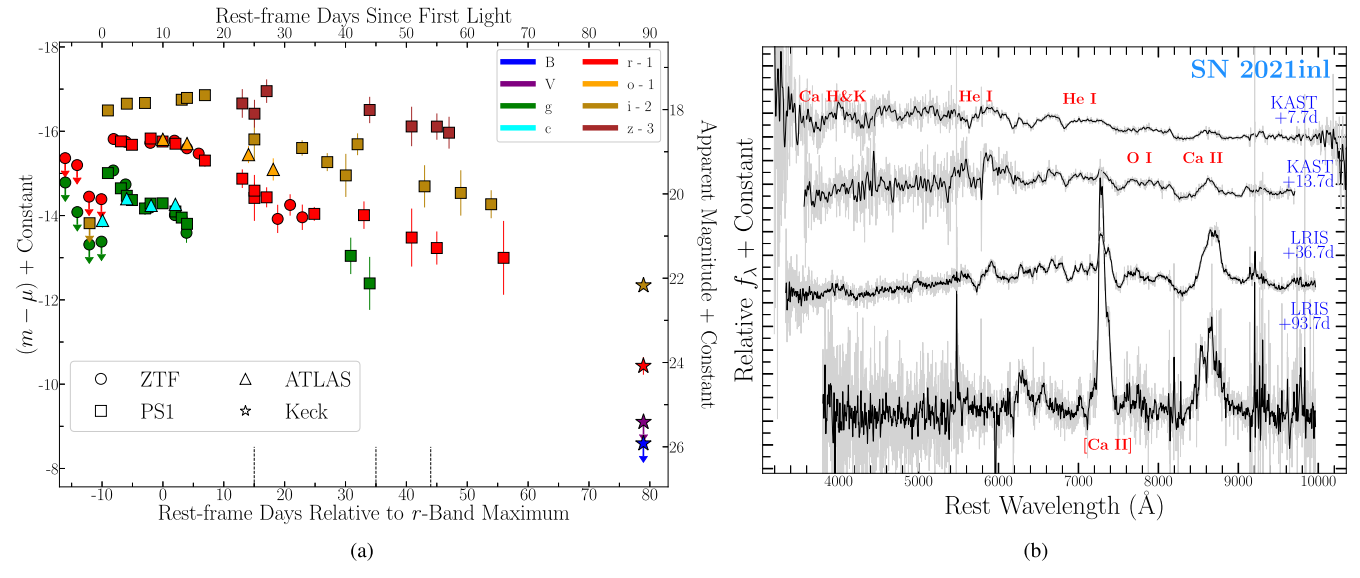


Figure 3. (a) Optical/NIR light curve of SN 2021inl with respect to second r-band maximum ($\delta t \approx 10$ days). Peak of primary light-curve peak occurs at phase $\delta t \approx 2$ days. Observed photometry presented in AB magnitude system. ATLAS data/ 3σ upper limits are presented as triangles, PS1/YSE as squares, Swift as diamonds, ZTF as circles, and Keck/LRIS as stars. The epochs of our spectroscopic observations are marked by black dashed lines. (b) Spectral observations of SN 2021inl with phases (blue) marked with respect to explosion. Raw spectra are shown in gray, and smoothed spectra with black lines. (The data used to create this figure are available.)

2.2. Optical/NIR spectroscopy

In Figures 4 and 3(b), we present the complete series of optical spectroscopic observations of SN 2021gno and SN 2021inl from δ t=3-84 days and δ t=25-111 days relative to explosion, respectively. A full log of spectroscopic observations is presented in Appendix Tables A2 and A4.

SNe 2021gno and 2021inl were observed with Shane/Kast (Miller & Stone 1993) and Keck/LRIS (Oke et al. 1995) between δ t=3-54 days and δ t=25-111 days relative to explosion, respectively. For all these spectroscopic observations, the standard CCD processing and spectrum extraction were accomplished with IRAF. The data were extracted using the optimal algorithm of Horne (1986). Low-order polynomial fits to calibration-lamp spectra were used to establish the wavelength scale, and small adjustments derived from night-sky lines in the object frames were applied. We employed custom IDL routines to flux calibrate the data and remove telluric lines using the well-exposed continua of the spectrophotometric standard stars (Wade & Horne 1988; Foley et al. 2003). Details of these spectroscopic reduction techniques are described in Silverman et al. (2012).

Spectra of SN 2021gno were also obtained with the Alhambra Faint Object Spectrograph (ALFOSC) on The Nordic Optical Telescope (NOT), as well as Binospec on MMT, and SpeX at the NASA Infrared Telescope Facility (IRTF). All of the spectra were reduced using standard techniques, which included correction for bias, overscan, and flat-field. Spectra of comparison lamps and standard stars acquired during the same night and with the same instrumental setting have been used for the wavelength and flux calibrations, respectively. When possible, we further removed the telluric bands using standard stars. Given the various instruments employed, the data-reduction steps described above have been

applied using several instrument-specific routines. We used standard IRAF commands to extract all spectra.

2.3. X-Ray Observations with Swift-XRT

The X-Ray Telescope (XRT; Burrows et al. 2005) on board the Swift spacecraft (Gehrels et al. 2004) started observing the field of SN 2021gno from 2021 March 20 to 2021 November 6 (δ t = 0.81–233.6 days since explosion with a total exposure time of 28.8 ks, IDs 14199 and 14214). We analyzed the data using HEAsoft v6.26 and followed the prescriptions detailed in Margutti et al. (2013), applying standard filtering and screening. A bright source of X-ray emission is clearly detected in each individual observation with significance of >3 σ against the background in the first two epochs (δ t = 0.81–1.14 days; total exposure time of 4.73 ks) and count rates of (3.8 \pm 1.6) \times 10⁻³ and (2.3 \pm 1.1) \times 10⁻³ c s⁻¹, respectively. Given how close in time the first XRT observations are to one another, we chose to merge the two event files and use the combined epoch for analysis of the X-ray spectrum.

To test the validity of the X-ray emission observed in SN 2021gno, we first employ a binomial test to understand the likelihood that the fading-X-ray emission was a chance coincidence. In this test, we compared the observed counts in the combined early time epoch to a late-time, template XRT image (3.6 ks) of the explosion site at ~234 days. We find a probability of fading-X-ray emission of only ~0.34%, further indicating that the observed X-ray photons were in fact derived from the SN at early times. Furthermore, in the template image, no X-ray emission is detected above the background level at later phases. The complete X-ray light curve is presented in Figure 5(a).

From the merged event file at $t \le 2.1$ days, we extracted a spectrum using a 15" region centered at the location of SN 2021gno. We find that the X-ray spectrum of the SN emission has a best-fitting photon index $\Gamma = 0.7 \pm 0.5$ (1 σ error) corresponding to an unabsorbed 0.3–10 keV flux of

https://github.com/msiebert1/UCSC_spectral_pipeline

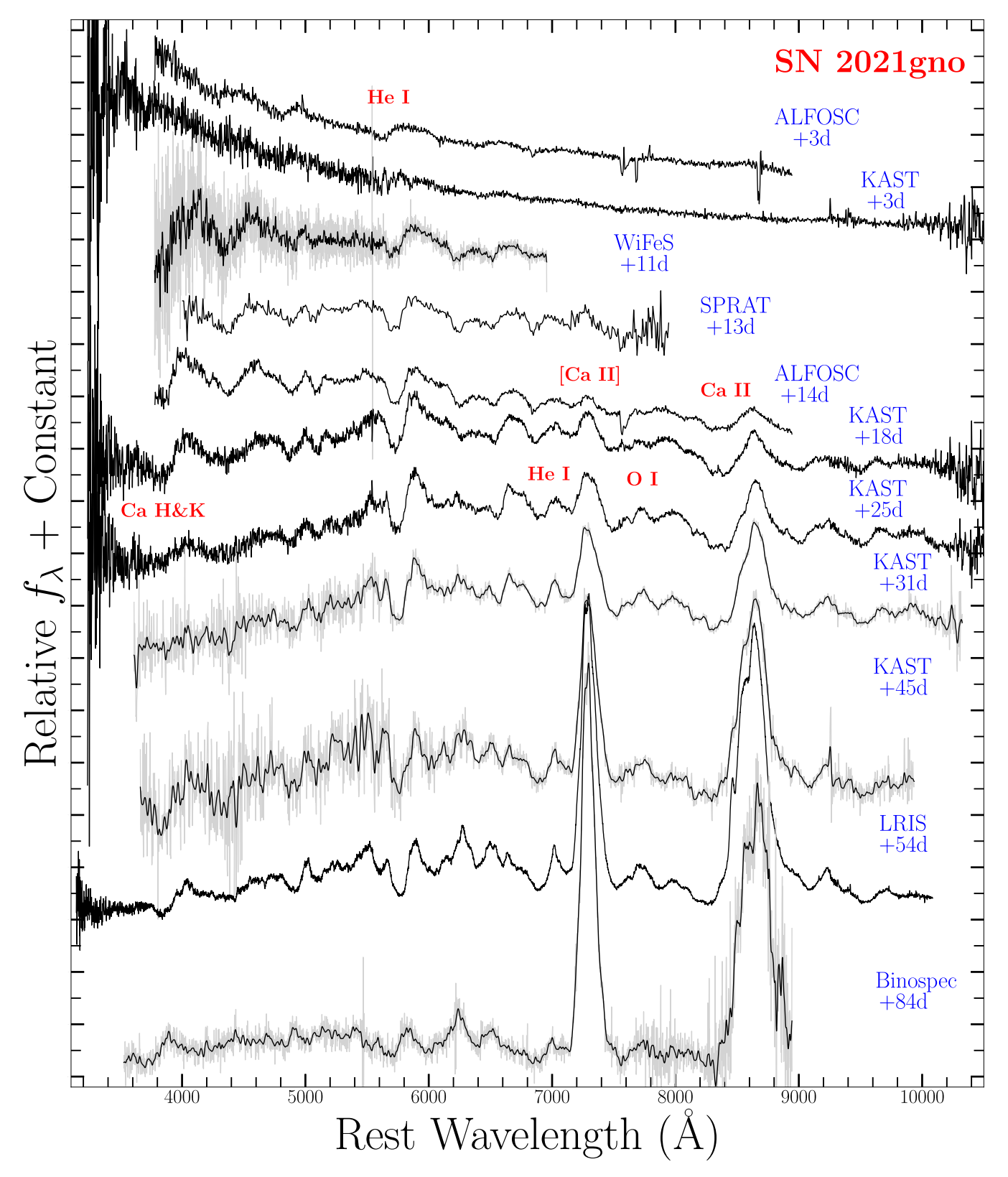


Figure 4. Spectral observations of SN 2021gno with phases (blue) marked with respect to explosion. Raw spectra are shown in gray, and smoothed spectra with black lines

(The data used to create this figure are available.)

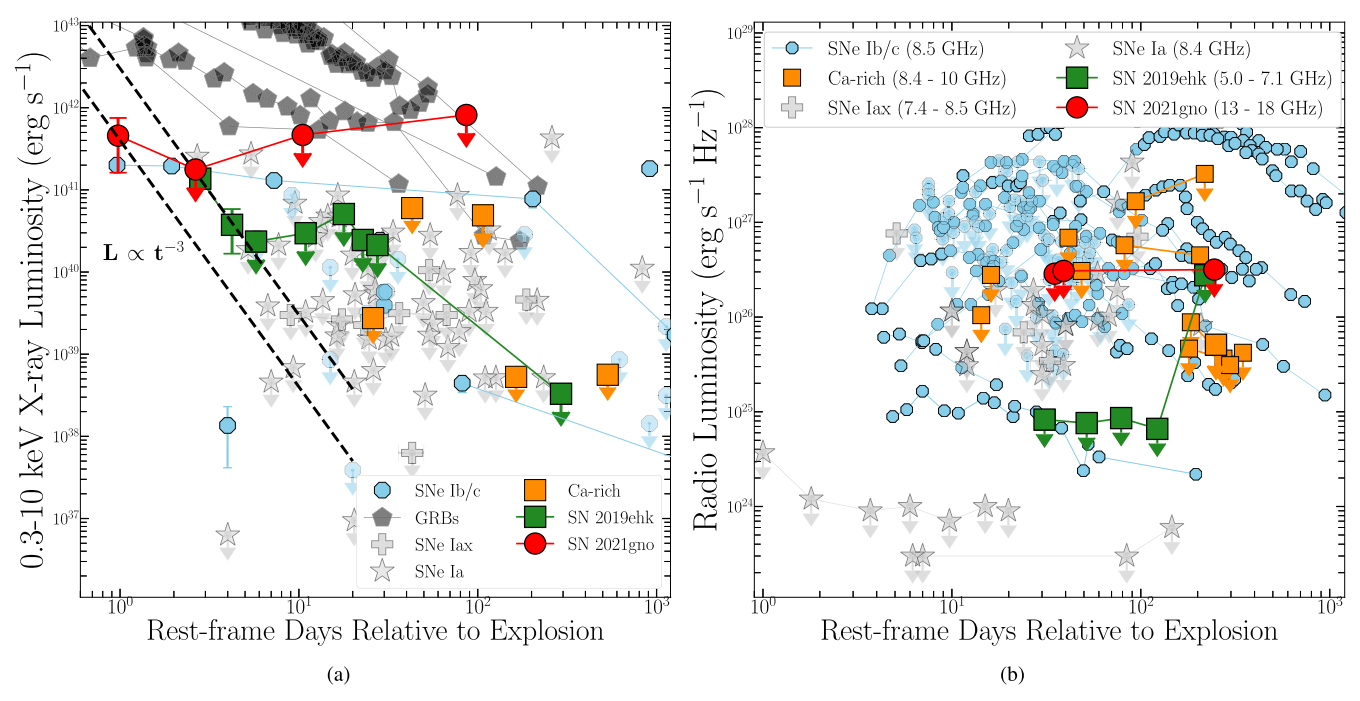


Figure 5. (a) X-ray light curve of SN 2021gno (red circles) and other thermonuclear transients, e.g., SNe Iax (gray plus signs), SNe Ia (gray stars), and CaSTs (orange squares). Core-collapse SNe Ib/c are shown as light-blue octagons and GRBs are displayed as black polygons. The decline rate of SN 2019ehk's X-ray emission (green squares; $L_x \propto t^{-3}$) is shown as a black dashed line, which is also consistent with SN 2021gno's decline rate (black dashed line). (b) Radio nondetections of SN 2021gno (red circles) compared to nondetection limits of thermonuclear SNe and SNe Ib/c.

 $F_x = (4.1 \pm 2.2) \times 10^{-12} \, \mathrm{erg \, s^{-1} cm^{-2}}$. No evidence for intrinsic neutral hydrogen absorption is found (NH_{MW} < 2.2 × $10^{18}\,\mathrm{cm^{-2}}$). The Galactic neutral hydrogen column density along our line of sight is NH_{MW} = $2.4\times10^{20}\,\mathrm{cm^{-2}}$ (Kalberla et al. 2005), which is used to account for the contribution of the host-galaxy in modeling the X-ray excess. We then use the best-fitting spectral parameters inferred from the merged observations to flux-calibrate the count-rate upper limits derived for the following epochs (Table A1). Given the distance to SN 2021gno, these measurements indicate a steeply decaying, large X-ray luminosity of $L_x \le 4.6 \times 10^{41} \, \mathrm{erg \, s^{-1}}$ at $t \le 2.1$ days (Figure 5), rivaling even the gamma-ray-burst SN, 1998bw (Kouveliotou et al. 2004). This very early time observation represents only the second X-ray detection in a CaST, the first being SN 2019ehk, which showed luminous rapidly fading-X-ray emission at $t \le 4.2$ days since explosion (WJG20a). Furthermore, SN 2021gno's decay in X-ray luminosity is consistent with the steep light-curve slope of $L_x \propto t^{-3}$ found in SN 2019ehk. However, because SN 2021gno has one X-ray detection, it is important to note that its X-ray decline rate could vary differently than that observed in SN 2019ehk.

The hard $0.3-10\,\mathrm{keV}$ X-ray spectrum of SN 2019ehk is suggestive of thermal bremsstrahlung emission with temperature $T>10\,\mathrm{keV}$. Consequently, we fit the SN 2021gno contribution with a bremsstrahlung spectral model with $T=20\,\mathrm{keV}$ and find an inferred emission measure of $EM=\int n_e n_I dV$ is $EM=(1.8\pm0.7)\times10^{64}\,\mathrm{cm}^{-3}$ (at $\delta t\approx1.0$ d), where n_e and n_I are the number densities of electrons and ions, respectively. Furthermore, in Section 7, we apply the estimated EM from the XRT detections to derive parameters of the CSM surrounding the progenitor system of SN 2021gno.

2.4. Radio Observations

We observed SN 2021gno with the Arcminute Microkelvin Imager Large Array (AMI-LA; Zwart et al. 2008; Hickish et al. 2018) on 2021 April 21, 25 and November 19 ($\delta t = 35$, 39, & 245 days since explosion) and found no evidence for radio emission from the SN. These data were all taken at a central frequency of 15.5 GHz across a 5 GHz bandwidth consisting of 4096 channels, which we average down to 8 for imaging. Radio-frequency-interference flagging and bandpass and phase reference calibration were performed using a custom reduction pipeline (Perrott et al. 2013). Additional flagging and imaging was performed in the Common Astronomy Software Applications (CASA; McMullin et al. 2007) package. For imaging we use natural weighting with a clean gain of 0.1. To measure the source flux density we use the CASA task IMFIT. The resolution of the AMI-LA (characteristic beam dimensions 400×3000) when observing at the decl. of J1820 means that the source is unresolved in all epochs. Details of each observation are presented in Appendix Table A3, and the derived-radio-luminosity limits for SN 2021gno are plotted in Figure 5(b).

3. Host-galaxy and Explosion Site

SN 2021gno is located 3.6 kpc in projection from the nucleus in the outer arm of its SBa type host-galaxy NGC 4165 (Figure 1(a)). We determine the host-galaxy oxygen abundance $12 + \log(O/H)$ by using an SDSS spectroscopic observation taken on 2004 April 20 of the galactic core; given the SN location, the metallicity at the explosion site is likely lower. Using a combination of line flux ratios ([O III] / H β and [N II]/H α) in Equations (1) amd (3) of Pettini & Pagel (2004), we

determine a range of host metallicities of $12 + \log(O/H) = 8.94 - 9.15$ dex $(1.03 - 1.06 \ Z_{\odot})$. Using the same spectrum, we find an $H\alpha$ emission line luminosity of $L_{H\alpha} = 8.7 \times 10^{39}$ erg s⁻¹, which corresponds to a star formation rate of SFR = $0.07 \ M_{\odot} \ \text{yr}^{-1}$ (Kennicutt 1998).

In order to understand the star formation rate (SFR) and metallicity at the exact location of SN 2021gno, we acquired an additional host spectrum at the explosion site using the Goodman spectrograph on SOAR on 2021 January 27, when the SN emission is not expected to be detected given its brightness at this phase and signal-to-noise ratio of the spectrum. We find no detectable host-galaxy emission lines at the SN location and perform a manual, optimal Gaussian extraction with a 6σ region, 3σ on each side of the SN location, which translates to distance of 0.22 kpc. We then derive a limit on the H α emission line luminosity by simulating a marginal detection as a Gaussian profile (FWHM = 100 km s^{-1}) with a peak flux of three times the spectrum's root-mean-square flux. We then calculate $L_{\rm H\alpha} < 4.3 \times 10^{36}~{\rm erg~s^{-1}}$ and a local SFR of $< 3.4 \times 10^{-5}~M_{\odot}~{\rm yr^{-1}}$. This estimate is consistent with the low SFR of $\sim 9.2 \times 10^{-5}~M_{\odot}~{\rm yr^{-1}}$ inferred from the explosion site of SN 2019ehk (WJG20a) and suggests that SN 2021gno is more likely to have originated from an older progenitor system (e.g., low-mass massive star or WD binary). Furthermore, the $H\alpha$ luminosity at the explosion site of SN 2019ehk is only consistent with the HII region luminosity at the location of ~20% of H-stripped SNe (Galbany et al. 2018; Kuncarayakti et al. 2018).

Similar to many other CaSTs, SN 2021inl is located at a large projected offset (\sim 23 kpc) from early-type, E/S0 hostgalaxy NGC 4923 (Figure 1(b)). While the explosion site indicates no star formation at the SN location, we also use an SDSS spectroscopic observation taken on 2007 February 22 of the galactic core to infer the properties of NGC 4923. To derive the properties of the host-galaxy, we model the SDSS spectrum as well as Galaxy Evolution Explorer All-Sky Survey Source Catalog (Seibert et al. 2012) UV, SDSS ugriz, and near-IR (NIR) Two Micron All Sky Survey (Jarrett et al. 2000) JHK_s photometry with the Fitting and Assessment of Synthetic Templates code (FAST; Kriek et al. 2009). Our model grid includes stellar initial mass functions by Salpeter (1955) and Chabrier (2003), star formation history that is exponentially decreasing, a delayed function, and the stellar population libraries presented by Bruzual & Charlot (2003) and Conroy et al. (2009). For models without host-galaxy dust reddening, we find a total stellar mass of $M_{\star} \approx (4.6 - 7.6) \times 10^{10} M_{\odot}$, metallicity of $Z \approx Z_{\odot}$ and SFR $\lesssim 10^{-5} M_{\odot} \text{ yr}^{-1}$. We also find consistent M_{\star} and Z measurements within a grid of models that included dust $(A_V = 0.6)$, but all models found an SFR = 0. Overall, these models indicate that SN 2021inl, given its large offset from a host with no apparent star formation, is not from a massive star progenitor.

4. Optical Light-curve Analysis

4.1. Photometric Properties

SNe 2021gno and 2021inl are the fourth and fifth confirmed CaSTs with clearly defined double-peaked light curves as shown in Figures 2 and 3(a), respectively. The other double-peaked objects in the present CaST sample are iPTF16hgs (De et al. 2018a), SN 2018lqo (De et al. 2020), and SN 2019ehk (Jacobson-Galán et al. 2020a; Nakaoka et al. 2021; De et al. 2021). Similar to other

double-peaked SNe, we define the phase of these SNe relative to both the secondary, "Nickel-powered" peak and to explosion as defined at the end of Section 1. For both CaSTs, we calculate the time of maximum by fitting a third-order polynomial to g- and r-band photometry. For SN 2021gno, we find best-fit g- and r-band peak absolute magnitudes of $M_g = -14.90 \pm 0.03$ mag at MJD 59305.2 \pm 0.6 and $M_r = -15.3 \pm 0.2$ mag at MJD 59307.6 \pm 0.6, respectively, resulting in an r-band rise-time of $t_r = 15.3 \pm 0.6$ days. For SN 2021inl, we find best-fit g- and r-band peak absolute magnitudes of $M_g = -14.3 \pm 0.1$ mag at MJD 59318.6 \pm 0.1 and $M_r = -14.8 \pm 0.2$ mag at MJD 59317.4 \pm 0.1, respectively, resulting in an r-band rise-time of $t_r = 8.04 \pm 0.10$ days.

In Figure 7, we present r- and g-band light-curve comparisons of SNe 2021gno and 2021inl to a sample of confirmed CaSTs. Overall, both objects have a consistent lightcurve evolution to other CaSTs, e.g., $t_r \lesssim 15$ days, $M_{\rm peak} > -16.5$ mag, and fast-decaying post-maximum photometry. Both SNe are among the lowest-luminosity events compared to other CaSTs, with SN 2021inl being ∼1 mag fainter than SNe 2005E (Perets et al. 2010) and 2019ehk (Jacobson-Galán et al. 2020a; Nakaoka et al. 2021) and \sim 2 mag less luminous than the peculiar "Calcium-strong" SN 2016hnk (Galbany et al. 2019; Jacobson-Galán et al. 2020b). Despite being intrinsically fainter, SN 2021gno's overall photometric evolution is most similar to SN 2019ehk and iPTF16hgs (De et al. 2018a); all three objects contain double-peaked light curves, as well as consistent rise-times and post-peak decline rates in both g and r bands. SN 2021inl's post-maximum decline is also consistent with SNe 2019ehk, 2021gno, and iPTF16hgs, with all objects exhibiting a relatively rapid decay in g-band flux following the Ni-powered SN peak. Additionally, we compare the g-r colors of SNe 2021 gno and 2021 inl to a CaST sample in Figure 6. Same as the photometric evolution, the overall g-r color evolution of these two objects at $\delta t < 70$ days post peak is quite consistent with the colors typically observed in other CaSTs. Similar to other objects observed early and with high-cadence observations (e.g., iPTF16hgs, SN 2019ehk), SNe 2021gno and 2021inl display blue colors at the start of their evolution (g - r < 0 mag), but quickly transform into instrinsically red explosions (g - r > 1 mag) following SN peak.

4.2. Bolometric Light Curve

For SN 2021gno, we construct a bolometric light curve by fitting the ZTF, PS1, Nickel, ATLAS, and Swift photometry with a blackbody model that is dependent on radius and temperature. The extremely blue UV colors and early time color evolution of SN 2021gno during its first light peak impose nonnegligible deviations from the standard Swift-UVOT count-to-flux conversion factors. We account for this effect following the prescriptions by Brown et al. (2010). Each spectral energy distribution (SED) of SN 2021gno was generated from the combination of multicolor UV/optical/ NIR photometry in the w2, m2, w1, u, b, v, g, c, o, r, i, and zbands (1500-10,000 Å). Similarly, for SN 2021inl, we construct a bolometric light curve by fitting the ZTF, PS1, Nickel, and ATLAS photometry with the same blackbody model to multiband g, c, o, r, i, and z bands (3000–10,000 Å). For both SNe, we extrapolated between light-curve data points using a low-order polynomial spline in regions without complete color information. All uncertainties on blackbody radii and temperature were calculated using the covariance matrix generated by

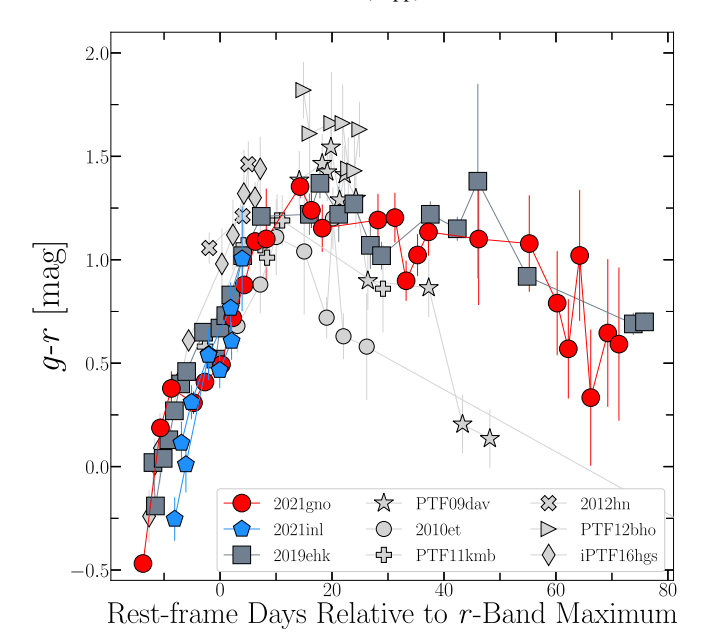


Figure 6. *g-r* color comparison of SN 2021gno (red circles), SN 2021inl (blue polygons), and current sample of CaSTs. All photometry has been extinction corrected

the SED fits. For the secondary, Nickel-powered light-curve peak, we find the peak bolometric luminosities of $(4.12 \pm 1.57) \times 10^{41} \, \mathrm{erg \, s^{-1}}$ and $(2.37 \pm 0.05) \times 10^{41} \, \mathrm{erg \, s^{-1}}$ for SN 2021gno and SN 2021inl, respectively.

In Figures 8(a)/(b), we present the bolometric light curves of SNe 2021 gno and 2021 inl, in addition to their blackbody radius and temperature evolution in Figure 9. In both figures, we also present the bolometric luminosities, blackbody radii, and temperatures of CaST SN 2019ehk (WJG20a). Overall, both SNe are less luminous than SN 2019ehk throughout all of their bolometric evolution except the very first data point of the first light-curve peak where the luminosities are comparable. However, the post-peak bolometric decline in SNe 2021gno and 2021inl is consistent with the rate observed in SN 2019ehk; all of these objects decline faster than the typical decay of $^{56}\text{Co} \rightarrow ^{56}\text{Fe}$ that assumes complete trapping of γ -rays. Furthermore, as shown in Figure 9, the blackbody temperature of SNe 2019ehk, 2021gno, and 2021inl are all nearly identical throughout the early time evolution, $\delta t < 70$ days since explosion. However, the blackbody radius of SN 2019ehk is larger than both SNe throughout their evolution, while SN 2021gno and SN 2021inl are consistent with one another for most early time epochs. Additionally, it should be noted that the blackbody approximation may not be appropriate when the emission lines (e.g., Ca II) begin to dominate the spectrum of SNe 2021gno and 2021inl, which occurs t > 40 days after explosion. Consequently, a blackbody assumption for these objects in those phases is most likely an oversimplification and could result in additional uncertainty on the presented bolometric luminosities.

For SN 2021gno, the earliest inferred blackbody radius is $\sim 9 \times 10^{13}$ cm ($\sim 1300\,R_\odot$) at $\delta t = 0.84$ days since explosion. This suggests a compact progenitor star with radius $R_\star \lesssim 10-100\,R_\odot$, which allows for the first detected blackbody radius to be reached given a shock velocity of $v_s \approx 1.2 \times 10^4\,\mathrm{km\,s^{-1}}$. Similarly, the first blackbody radius of $\sim 10^{14}\,\mathrm{cm}$ ($\sim 1400\,R_\odot$) in SN 2021inl at $\delta t = 0.97$ days also allows for a compact progenitor radius of $R_\star \lesssim 10-100\,R_\odot$ for

 $v_s \approx 1.2 \times 10^4 \, \mathrm{km \, s^{-1}}$. Similar inferences that we made for SN 2019ehk whose initial blackbody radius at $\delta t \approx 0.4$ days after explosion rule out an extended progenitor. Furthermore, in all three SNe, WD progenitors are still permitted given the time it would take the SN shock to reach the first blackbody radii from a much smaller initial stellar radius.

To determine physical parameters of both SNe such as ejecta mass (M_{ei}) , kinetic energy (E_k) , and ⁵⁶Ni mass (M_{Ni}) , we model both bolometric light curves with the analytic expressions presented in Appendix A of Valenti et al. (2008) and in Wheeler et al. (2015). Same as in SN 2019ehk, we exclude the first light-curve peak and model two distinct phases of the light curve: photospheric ($\delta t < 30$ days; Arnett 1982) and nebular $(\delta t > 40 \text{ days}; \text{ Sutherland & Wheeler 1984}; \text{ Cappellaro et al.}$ 1997). The analytic formalism applied in this modeling selfconsistently implements the possibility of incomplete γ -ray trapping, and a typical opacity of $\kappa = 0.1 \, \mathrm{cm}^2 \, \mathrm{g}^{-1}$ is applied in each model. Furthermore, we correct for the known degeneracy between kinetic energy and ejecta mass (e.g., see Equation (1) in WJG20a) by applying photospheric velocities of $v_{\rm ph} \approx$ $6000 \, \mathrm{km \, s^{-1}}$ for SN 2021gno and $v_{\mathrm{ph}} \approx 7500 \, \mathrm{km \, s^{-1}}$ for SN 2021inl, both of which are derived from Si II absorption features in the SN spectra. For SN 2021gno, we find an ejecta mass of $M_{\rm ej} = 0.60 \pm 0.01 \, M_{\odot}$, kinetic energy of $E_{\rm k} = (1.3 \pm 0.2) \times 10^{50}$ erg, and ⁵⁶Ni mass of $M_{\rm Ni} = (1.20 \pm 0.02) \times$ $10^{-2}M_{\odot}$. For SN 2021inl, we calculate an ejecta mass of $M_{\rm ej} = 0.29 \pm 0.01 \, M_{\odot}$, kinetic energy of $E_{\rm k} = (9.6 \pm 0.4) \times 10^{49}$ erg, and $^{56}{\rm Ni}$ mass of $M_{\rm Ni} = (6.90 \pm 0.06) \times 10^{-3} M_{\odot}$. In both SNe, the photospheric and nebular model fits (shown in Figure 8) return consistent parameter values. We note that all uncertainties on these explosion parameters are purely statistical, and there are likely larger systematic errors derived from the construction of the bolometric light curve, as well as the assumed opacity and velocity of the SN ejecta. Overall, the explosion parameters in SN 2021gno are very consistent with those derived for SN 2019ehk (WJG20a) despite a slightly lower M_{Ni} , which explains the larger luminosities observed in SN 2019ehk. However, SN 2021inl's explosion parameters are all lower than those observed in SNe 2019ehk and 2021gno, but are consistent with the values generally found in the CaST class (De et al. 2020). We compile all explosion parameters of SNe 2021gno and 2021inl, in addition to SN 2019ehk, iPTF16hgs, and the objects studied in De et al. (2020), in Appendix Table A5.

5. Optical/NIR Spectral Analysis

5.1. Spectroscopic Properties

The complete spectral series of SNe 2021gno and 2021inl is presented in Figures 4 and 3(b), both of which include obvious ion identifications for both SNe. During their photospheric phase, both SNe display prominent He I, O I, Ca II, Si II, and Fe-group element transitions; neither SNe showing evidence for detectable H I. In the first spectrum of SN 2021gno at +3 days post explosion, we find that all the broad features can be identified as fast-moving He I $\lambda\lambda$ 4471, 5016, 5876, 6678 profiles and find a consistent expansion velocity of $\sim 1.3 \times 10^4 \, \mathrm{km \, s^{-1}}$ from the minimum of the absorption profile. Based on the absorption profiles in the SN 2021gno maximum light spectrum, we find characteristic ejecta velocities of $\sim 7000 - 8000 \, \mathrm{km \, s^{-1}}$ for He I, $\sim 6500 \, \mathrm{km \, s^{-1}}$ for Si II, and $\sim 7000 \, \mathrm{km \, s^{-1}}$ for Ca II. We find similar expansion

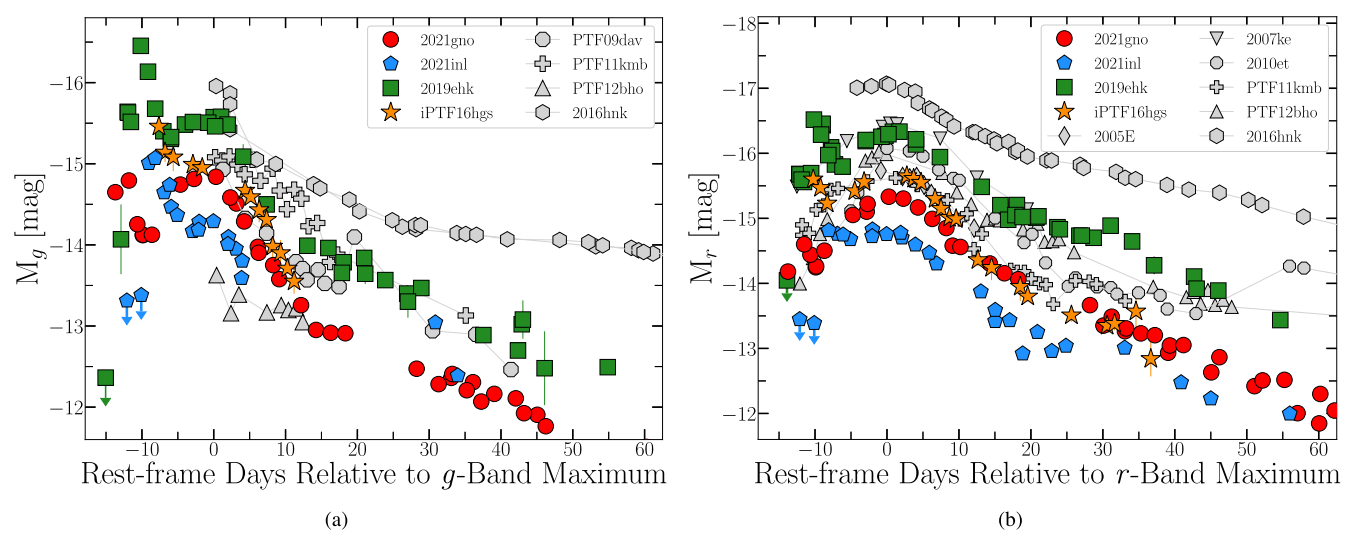


Figure 7. (a) Early time *g*-band comparison of SN 2021gno (red circles), SN 2021inl (blue polygons), and classified CaSTs (Sullivan et al. 2011; Lunnan et al. 2017; De et al. 2018a; Jacobson-Galán et al. 2020a, 2020b). The peculiar, *calcium-strong* SN 2016hnk also presented for reference (gray hexagons). SNe 2021gno and 2021inl are the fourth and fifth objects in this class to show a double-peaked light curve, iPTF16hgs (orange stars), SN 2019ehk (green squares), and SN 2018lqo (De et al. 2020) being the first three confirmed cases. (b) *r*-band comparison of SN 2021gno (red circles), SN 2021inl (blue polygons), and classified CaSTs.

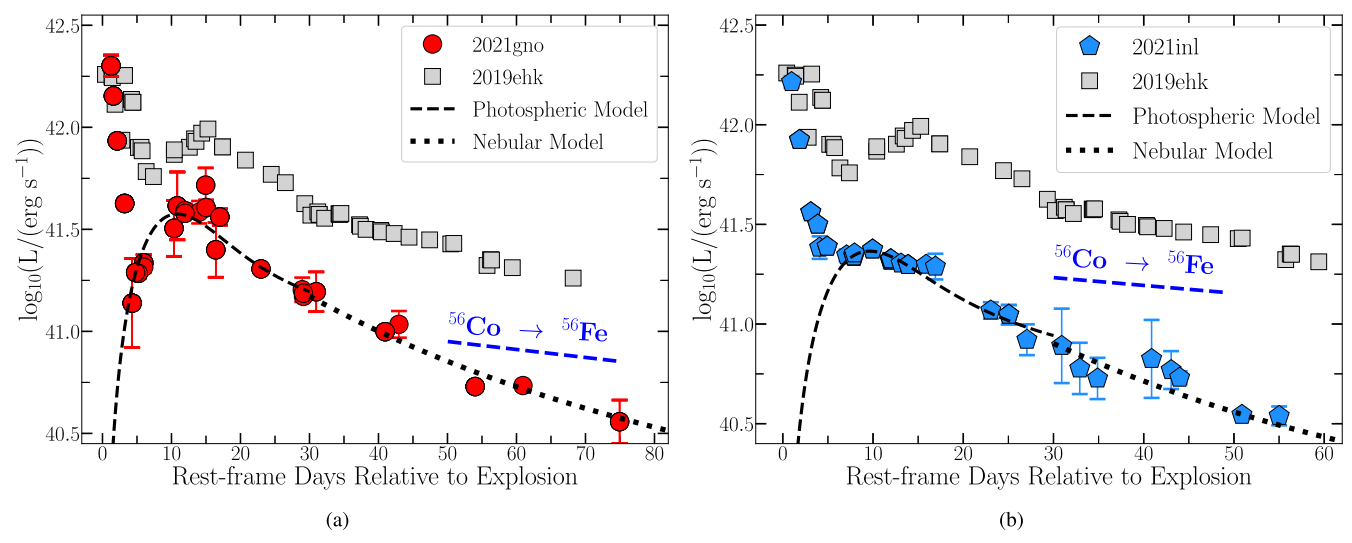


Figure 8. (a) Bolometric light curves of SNe 2021gno (red circles) and 2019ehk (gray squares). Secondary, 56 Ni-powered peak in SN 2021gno is at a phase of $\delta t \approx 10$ days, while the primary peak from shock cooling emission or CSM interaction is during phases $\delta t < 5$ days. Photospheric light-curve model for the early time light curve of SN 2021gno (Section 4.2) is plotted as dashed black line. Modeling of the nebular phase data plotted as dotted black line. Blue dashed line shows the luminosity decline rate for a radioactive-decay-powered light curve with complete γ-ray trapping. (b) Bolometric light curves of SNe 2021inl (blue polygons) and 2019ehk (gray squares). Secondary, 56 Ni-powered peak in SN 2021inl is at a phase of $\delta t \approx 10$ days.

velocities in SN 2021inl, such as $\sim (1-1.2) \times 10^4 \mathrm{km \ s^{-1}}$ for He I, $\sim 7500 \ \mathrm{km \ s^{-1}}$ for Si II, and $\sim 8000 \ \mathrm{km \ s^{-1}}$ for Ca II. Overall, the ejecta velocities estimated for both SNe are consistent with the ion velocities found for SN 2019ehk (WJG20a) and other CaSTs (Kasliwal et al. 2012; Lunnan et al. 2017; De et al. 2020).

In Figure 10, we present the IR spectra of SN 2021gno at +10 days after second maximum compared to SN 2019ehk at +38 days; these two observations being the only confirmed IR spectra of a CaST during the photospheric phase. The IR spectrum of SN 2021gno shows nearly identical transitions to SN 2019ehk, both objects showing clear P-Cygni profiles of Ca II, He I, C I, and Mg I. Furthermore, the expansion velocities of these transitions are consistent with the ejecta velocities

derived from optical spectra, e.g., $\sim 1.1 \times 10^4 \, \mathrm{km \, s^{-1}}$ for He I and $\sim 9000 \, \mathrm{km \, s^{-1}}$ for Ca II.

In Figure 11(a), we present early time spectral comparisons of SNe 2021gno and 2021inl to other CaSTs near (second) maximum light. Overall, both SNe show consistent spectral features to all plotted CaSTs, but are most similar to SN 2019ehk and iPTF16hgs at this phase. All four objects show prominent He I and Ca II transitions as well as the fast emergence of a [Ca II] emission profile relative to peak. Furthermore, we compare the midtime spectra of SN 2021gno at +19 days to SNe 2005E, 2007ke, and 2019ehk in Figure 11(b). At this phase, SN 2021gno shows nearly identical transitions to these CaSTs such as prominent [Ca II] and marginal [O I]. These spectral comparisons are further

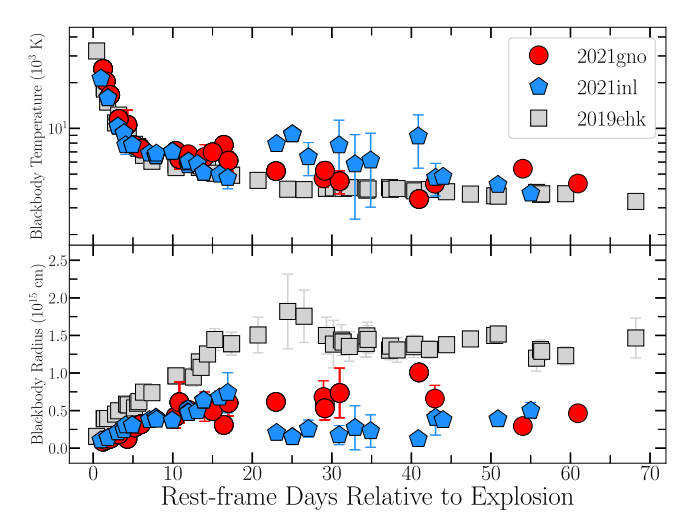


Figure 9. Blackbody radii (bottom panel) and temperatures (top panel) derived from SED modeling of all multicolor optical photometry from SNe 2021gno (red circles), 2021inl (blue polygons), and 2019ehk (gray squares).

indication that both SNe 2021gno and 2021inl are clear members of the CaST class.

5.2. Inferences from Nebular Phase Spectroscopy

Similar to other CaSTs, SNe 2021gno and 2021inl show a fast transition from the photospheric to the optically thin regime where their spectra become dominated by forbidden emission lines such as [Ca II] and [O I] (Figure 12). For SN 2021gno, the transition to the nebular regime occurs at \sim 13–18 days after explosion, which is evident from the presence of [Ca II] emission in the early time spectra; this transition then comes to dominate the spectra at later phases (Figure 4). Despite the lower-cadence spectroscopic observations, a similar behavior is observed in SN 2021inl, whose first spectrum at +8 days shows marginal evidence for [Ca II] emission, which later becomes the dominant transition by +94 days (Figure 3(b)).

Once in the optically thin regime, we calculate [Ca II]/[O I] line flux ratio, which, if greater than 2, is a common classifier of CaSTs and present this quantity in Figure 13(a) for both SNe. Based on this metric, we find that both objects are significantly rich in [Ca II] emission as shown by a maximum line flux ratio of [Ca II]/[O I] ≈ 10 . These flux ratios are consistent with other CaSTs presented in Figure 13(a), but neither SN has as large of a [Ca II]/[O I] ratio as SN 2019ehk, which remains the member of CaST with the largest [Ca II] flux relative to [O I] at all phases. Furthermore, in Figures $\frac{13(b)}{(c)}$, we present the velocity profiles [Ca II] and [O I] of SNe 2021gno and 2021inl, respectively, with the O emission scaled to match the Ca feature. We find that, in both objects, these forbidden line transitions are consistent in shape and indicate [Ca II] and [O I] expansion velocities of ~5000-6000 km s⁻¹ based on the FWHM of the emission profiles.

In order to understand the Ca and O abundance in each explosion, we apply a similar analysis to that outlined in Section 6.3 of WJG20a where the observed luminosities of [Ca II] and [O I] are related to the populations of the excited states, ion number densities ($n_e > 10^7$ cm⁻³), and Einstein A

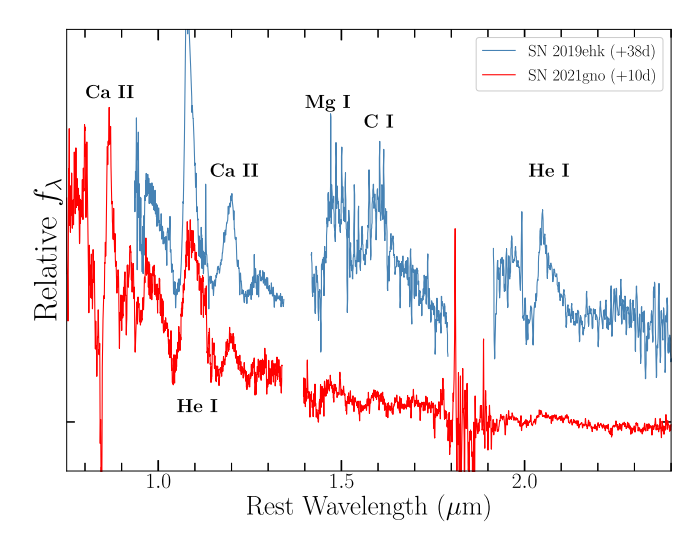


Figure 10. SPEX NIR spectrum (red) of SN 2021gno at +10 days relative to second B-band peak. NIR spectrum of SN 2019ehk shown in blue (WJG20a); these being the only early time NIR spectra taken of CaSTs. Prominent line transitions are marked in black.

coefficient values of each ion:

$$L_{\rm [OI]} = n_{\rm OI} A_{\rm [OI]} h \nu_{\rm [OI]} (5/14) e^{-22000/T}$$
 (1)

$$L_{\text{[Ca II]}} = n_{\text{Ca II}} A_{\text{[Ca II]}} h \nu_{\text{[Ca II]}} (10/11) e^{-19700/T}$$
 (2)

where $h\nu$ is the photon energy, n is the ion number density, $A_{\rm [Ca~II]}=2.6~{\rm s}^{-1},~A_{\rm [Ca~II]}\approx 390A_{\rm [OI]},$ the exponentials are the Boltzmann factors (T is in K), and the numerical factors are statistical weights. To find the ion number densities and subsequent masses in each SN, we first estimate the forbidden line luminosities to be $L_{\rm [OI]}=3.9\times10^{38}~{\rm erg~s}^{-1}$ and $L_{\rm [Ca~II]}=3.5\times10^{39}~{\rm erg~s}^{-1}$ for SN 2021gno ($\delta t=84~{\rm days~since}$ explosion), and $L_{\rm [OI]}=8.2\times10^{38}~{\rm erg~s}^{-1}$ and $L_{\rm [Ca~II]}=3.6\times10^{39}~{\rm erg~s}^{-1}$ for SN 2021inl ($\delta t=111~{\rm days~since}$ explosion). In the analytic relations above, we choose to calculate Ca and O masses for a range of temperatures $T=5000-10^4~{\rm K}$, for completeness.

For SN 2021gno, we calculate O and Ca masses of $M(O) = (0.6-6) \times 10^{-2} M_{\odot}$ and $M(Ca) = (1-9) \times 10^{-4} M_{\odot}$, for temperatures $T = 10^4 - 5000$ K. Similarly, for SN 2021inl, we find O and Ca masses of $M(O) = 0.01 - 0.1 M_{\odot}$ and $M(Ca) = (1-10) \times 10^{-4} M_{\odot}$, for $T = 10^4 - 5000$ K. These abundances are lower overall, but still somewhat consistent, to those found by WJG20a for SN 2019ehk, e.g., $M(O) = 0.10 M_{\odot}$ and $M(Ca) = 4 \times 10^{-3} M_{\odot}$. However, it should be noted that at these phases both SNe are not fully nebular, and therefore the derived masses may be lower than the true elemental masses in the explosion. Nevertheless, these mass estimates continue to prove that the *richness* of Ca emission in CaSTs is not due to a larger intrinsic amount of Ca relative to O, but rather it is likely the result of relative abundances and ionization temperatures in the inner, low-density ejecta.

6. Early Time Flux Excess

6.1. Observational Properties

Similar to other double-peaked CaSTs, the early time excess in flux above the 56 Ni-powered continuum is observed in all available UV/optical/NIR filters used to observe SNe 2021gno

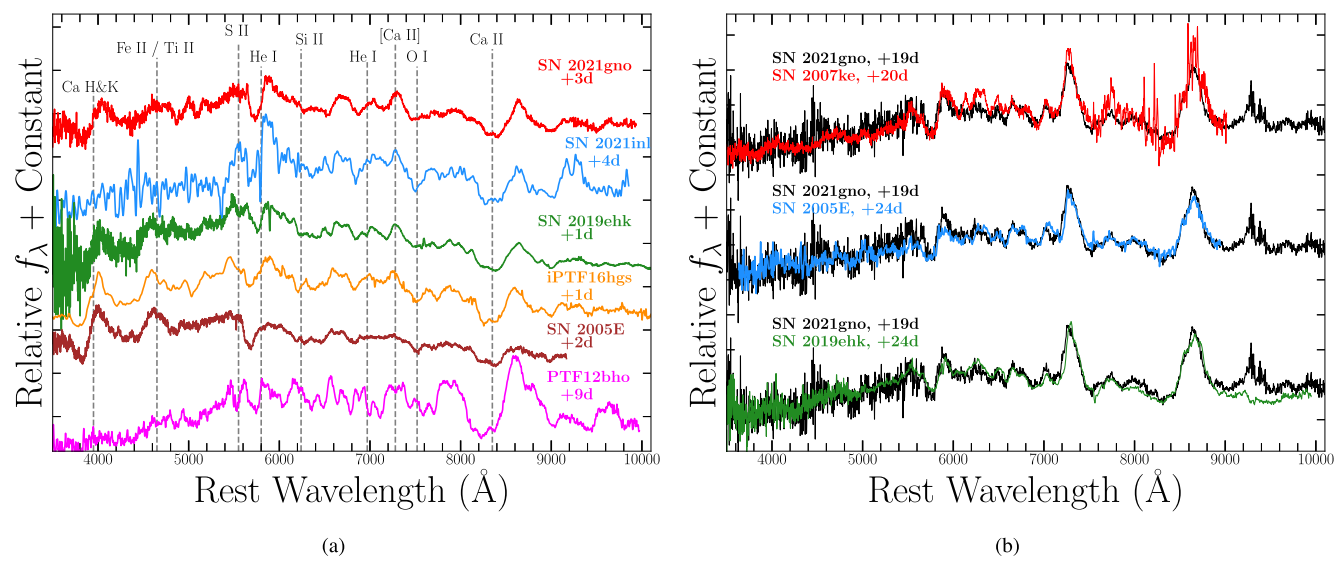


Figure 11. (a) Spectral comparison of SN 2021gno (red), SN 2021inl (blue), and other CaSTs near maximum light (Perets et al. 2010; Sullivan et al. 2011; Lunnan et al. 2017; De et al. 2018a). Common ions are marked by gray lines. (b) Direct spectral comparison of SN 2021gno (black) and CaSTs SNe 2007ke, 2005E, and 2019ehk at approximately the same phase (Perets et al. 2010; Lunnan et al. 2017). Almost every line transition is matched between spectra, with SN 2021gno showing similar Ca II emission to all other objects.

and 2021inl. Additionally, these very early time observations of both SNe represent the only other instances where the initial rise of the primary light-curve peak was recorded in a CaST, the first being in SN 2019ehk. In Figure 14, we present the g-r colors, as well as r- and g-band light curves of SNe 2019ehk, 2021gno, 2021inl, and iPTF16hgs during their primary light-curve phase.

For all four double-peaked CaSTs in Figure 14(a), the g-r color evolution during the flux excess follows a consistent trend: all objects show a linear increase in color following first detection, and all begin with quite blue colors, e.g., g-r<-0.2 mag. Seemingly, the physical process behind this early time flux excess is responsible for a retention of high blackbody temperatures and, consequently, blue colors until the SN emission becomes dominated by energy injection from 56 Ni decay.

As shown in Figures 14(b)/(c), SN 2019ehk remains the most luminous double-peaked CaST, with its flux excess peaking at $M \approx -16.5$ mag in g and r bands. SNe 2021gno and 2021inl are lower-luminosity events compared to SN 2019ehk and iPTF16hgs, with their primary g- and r-band light curves peaking at $M \approx -14.8$ mag and $M \approx -15.2$ mag, respectively. Furthermore, the light-curve slopes during this phase varies between all CaSTs. SN 2021gno shows a g-band decline rate of $\Delta m(g)_5 = 0.52$ mag during the ~ 5 day primary peak duration while SN 2021inl has a decline rate of $\Delta m(g)_7 = 0.64$ mag. Additionally, SN 2019ehk has a very fast decline rate of $\Delta m(g)_5 = 1.1$ mag during its largest flare in early time flux, while iPTF16hgs has a similarly rapid decline of $\Delta m(g)_3 = 0.75$ mag.

6.2. Shock Breakout and Envelope Cooling Model

For stellar progenitors with an extended envelope, the energy deposited by the passage of a shock through their envelopes manifests in detectable shock cooling emission (SCE) on a timescale of $t \lesssim$ days after shock breakout. This process has been modeled both analytically (e.g., Nakar & Piro 2014; Piro 2015) and numerically (e.g., Sapir & Waxman 2017;

Piro et al. 2017, 2021), these models being highly effective at reproducing the early time double-peaked light curves of SNe IIb (e.g., SNe 1993J, 2011dh, 2016gkg, 2017jgh; Wheeler et al. 1993; Arcavi et al. 2011, 2017; Piro et al. 2017; Armstrong et al. 2021), superluminous SNe (e.g., DES14X3-taz; Smith et al. 2016), SNe Ic (e.g., SNe 2014ft, 2020bvc, 2020oi; De et al. 2018b; Ho et al. 2020; Gagliano et al. 2022), fast-risers (e.g., 2019dge; Yao et al. 2020), and CaSTs (e.g., iPTF16hgs, SN 2019ehk; De et al. 2018a; Nakaoka et al. 2021; Jacobson-Galán et al. 2020a). Furthermore, by fitting the primary light-curve peaks of these double-peaked SNe, information about the extended material around the progenitor star at the time of explosion can be derived, such as the envelope mass and radius, as well as the shock velocity.

In order to understand the physical origin of their early time flux excess, we fit the primary light-curve peaks of SNe 2021gno and 2021inl with models for SCE of extended material. We apply four models to fit the SN light curves: the original SCE model by Piro (2015) as well as the revised twocomponent formalism presented in Piro et al. (2021), in addition to the models of Sapir & Waxman (2017) who numerically model SCE from both red and blue supergiant, H-rich envelopes (polytropic index of n = 3/2 and n = 3, respectively). Presentation of the analytic expressions behind these models can be found in Arcavi et al. (2017) or Section 7.3 of WJG20a. Following the shock breakout, each model produces constraints on the envelope mass, M_e , envelope radius, R_e , the velocity of the envelope, v_e , and the time offset from explosion t_o (consistent with our explosion time estimate). In this analysis, we use emcee, a Python-based application of an affine invariant Markov Chain Monte Carlo with an ensemble sampler (Foreman-Mackey et al. 2013). We compile the best-fit parameter estimates from each model in Table A6.

In Figures 15 and 16, we present the best-fitting multicolor light curves of the aforementioned models for SNe 2021gno and 2021inl, respectively. We also present model bolometric light curves, as well as their blackbody temperatures and radii, in Figure 17 with respect to the SNe 2021gno and 2021inl data. In

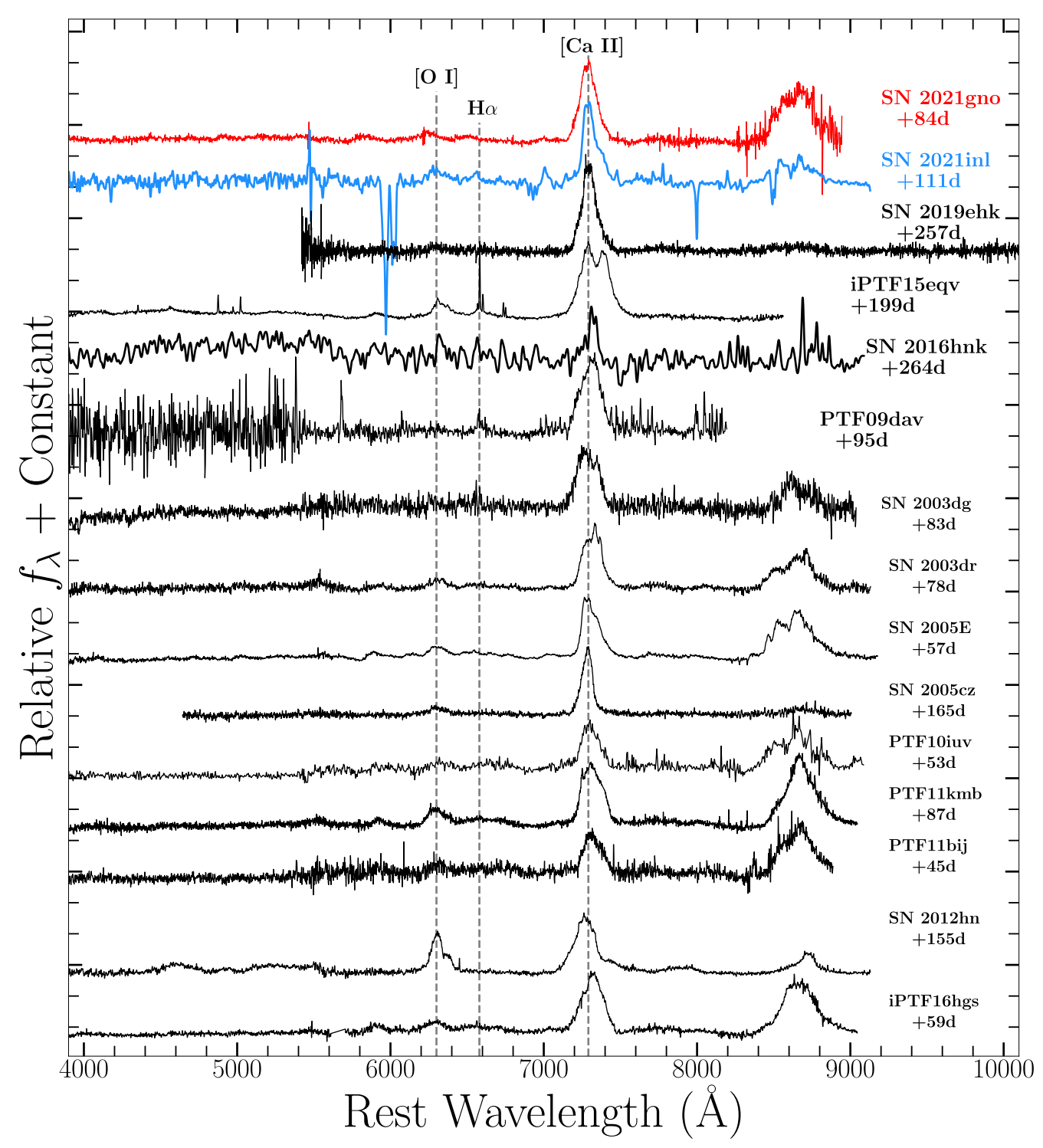


Figure 12. Nebular spectra of all confirmed CaSTs (Sullivan et al. 2011; Kasliwal et al. 2012; Foley 2015; Lunnan et al. 2017; Milisavljevic et al. 2017; Jacobson-Galán et al. 2020a, 2020b). Nebular spectra of SN 2021gno at +84 days and SN 2021inl at +111 days, shown in red and blue, respectively, both spectra further establishing these objects as CaSTs. Prominent [O I] and [Ca II] lines as well as $H\alpha$ marked by dashed gray lines.

general, we find that SCE can accurately reproduce the early time flux excess in both objects, with the models of Sapir & Waxman (2017) providing the best-fit and lowest χ^2 value overall. From all four model fits, the SN 2021gno light curve is best reproduced by an extended mass $M_e \approx 0.013-0.47\,M_\odot$ with radius $R_e \approx 27.5-385\,R_\odot$ and shock velocity $v_e \approx (4.5-7.8)\times 10^4 {\rm km\,s^{-1}}$. Furthermore, we find two best-fitting times of explosions: 59292.3 MJD for Piro (2015); Piro et al. (2021)

models; and 59293.01 MJD for Sapir & Waxman (2017) models; both values being consistent with the model-independent estimate of $t_{\rm exp}=59292.7\pm0.55$ MJD. Additionally, for SN 2021inl, we form best-fitting SCE model parameters of $M_e\approx0.02-1.61\,M_\odot$, $R_e\approx20.5-207\,R_\odot$, and $v_e\approx(4.5-7.8)\times10^4{\rm km~s}^{-1}$; there is no change to the original explosion date estimate. Lastly, we caution against using the M_e derived from the blue supergiant SCE model by Sapir & Waxman (2017) to best understand the progenitor

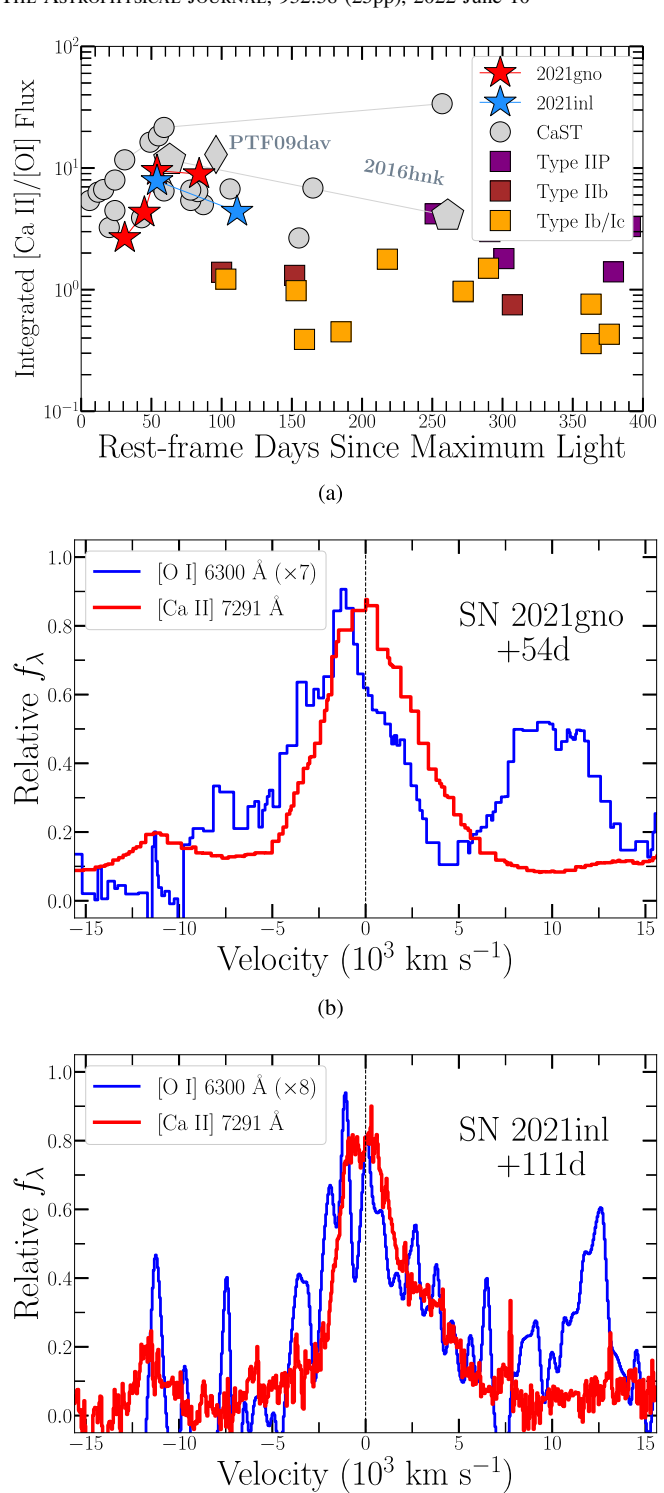


Figure 13. (a) Ratio of integrated [Ca II] and [O I] flux with respect to phase for SN 2021gno (red stars), SN 2021inl (blue stars), and current sample of CaSTs (gray circles, diamonds, and polygons), and assorted types of core-collapse SNe. All CaSTs, including SNe 2021gno and 2021inl, show [Ca II]/[O I] > 2. [Ca II]/[O I] values for all Type II/lbc objects from Milisavljevic et al. (2017). (b)/(c) Velocity profiles of [Ca II] $\lambda\lambda$ 7291,7324 (red) and scaled [O I] $\lambda\lambda$ 6300, 6364 (blue) in SN 2021gno at +54 days and SN 2021inl at +111 days post explosion.

(c)

environments of these CaSTs given that the estimated envelope mass is larger than the ejecta mass in SN 2021inl and a significant fraction of the mass of SN 2021gno, both scenarios being

unphysical in nature. We therefore conclude that the most physical range of best-fitting extended masses for both objects are $M_e = (1.5-4.5)\times 10^{-2}M_{\odot}$ for SN 2021gno and $M_e \approx 2.3\times 10^{-2}\,M_{\odot}$ for SN 2021inl; only the Piro (2015) model returned a mass that was not comparable in size, and consequently unphysical, to SN 2021inl's total ejecta mass.

In Figure 18, we attempt to compare the radius and mass of the extended material estimated from the SCE modeling of SNe 2021gno and 2021inl to other double-peaked events whose primary light-curve peak was modeled in a similar fashion. As shown in the plot, the SCE parameter space of all five double-peaked CaSTs is highly consistent: on average, these objects can be modeled with SCE from extended material that has a compact radius of $\sim 50-120 R_{\odot}$ and mass of $\sim 0.05 - 0.1 \, M_{\odot}$. Compared to SCE model parameters presented in the literature, CaSTs show a similar extended mass to fastrising events such as SN 2019dge (Yao et al. 2020) and SNe IIb (Wheeler et al. 1993; Arcavi et al. 2011, 2017; Piro et al. 2017; Armstrong et al. 2021), the latter typically exhibiting larger extended radii, likely indicating a more massive progenitor star than what produces CaSTs. Furthermore, the SCE parameter space of CaSTs is unlike that of SNe Ic (De et al. 2018b; Ho et al. 2020; Gagliano et al. 2022) and superluminous SNe (Smith et al. 2016), the former showing a much larger range of radii and smaller masses, while the latter is best fit by a much larger extended material mass and radius. However, we note that the parameters derived for all CaSTs presented were done using four separate SCE models (e.g., Piro 2015; Piro et al. 2021; Sapir & Waxman 2017), while other objects shown were only modeled with one of these formalisms. Therefore, a direct comparison of the SCE parameters may not be completely accurate.

6.3. CSM Interaction Model

In addition to the SCE model, we explore interaction of the explosion's shock with a circumstellar medium as a mechanism to explain the primary light-curve peaks of SNe 2021gno and 2021inl. We model the interaction as homologously expanding ejecta interacting with a detached CSM shell. In this picture, the CSM is sufficiently optically thick; the radiation becomes visible only after shock breakout from the outer edge of the CSM. The light curve is then powered by the resulting shock cooling emission of the swept up CSM and ejecta.

In this model, we assume a broken power-law ejecta with density profile $\rho_{\rm ej} \propto r^{-1}$ and $\rho_{\rm ej} \propto r^{-10}$ in the inner and outer ejecta, respectively; and assume the ejecta is expanding homologously with a kinetic energy of $E_{\rm sn}$. The CSM of mass $M_{\rm csm}$ extends from an inner radius $R_{\rm csm}$ with a width of $\Delta R_{\rm csm}$. The density profile follows a $\rho_{\rm csm} \propto r^{-2}$ profile out to $R_{\rm csm} + \Delta R_{\rm csm}$.

We run numerical simulations using the radiation hydrodynamics code Sedona (Kasen et al. 2006). The equations of radiation hydrodynamics are solved in a one-dimensional spherical symmetry using an implicit Monte Carlo radiative transfer (Roth & Kasen 2015) coupled to a moving mesh hydrodynamics code based off of Duffell (2016). We assume a gray electron-scattering opacity of $\kappa_{\rm es}=0.1~{\rm cm}^2~{\rm g}^{-1}$ and an absorptive opacity of $\kappa_{\rm abs}=\epsilon\kappa_{\rm es}$, with $\epsilon=10^{-3}$ to account for Compton thermalization. We assume $M_{\rm ej}=0.3-0.6\,M_{\odot}$ (i.e., $M_{\rm ej}$ for SN 2021gno and SN 2021inl, respectively), $E_{\rm sn}=(1-2)\times10^{50}~{\rm erg~s}^{-1}$ (i.e., E_k for SN 2021gno and SN 2021inl, respectively), $M_{\rm csm}=0.02\,M_{\odot}$, $R_{\rm csm}=10^{13}~{\rm cm}$, $\Delta R_{\rm csm}=$

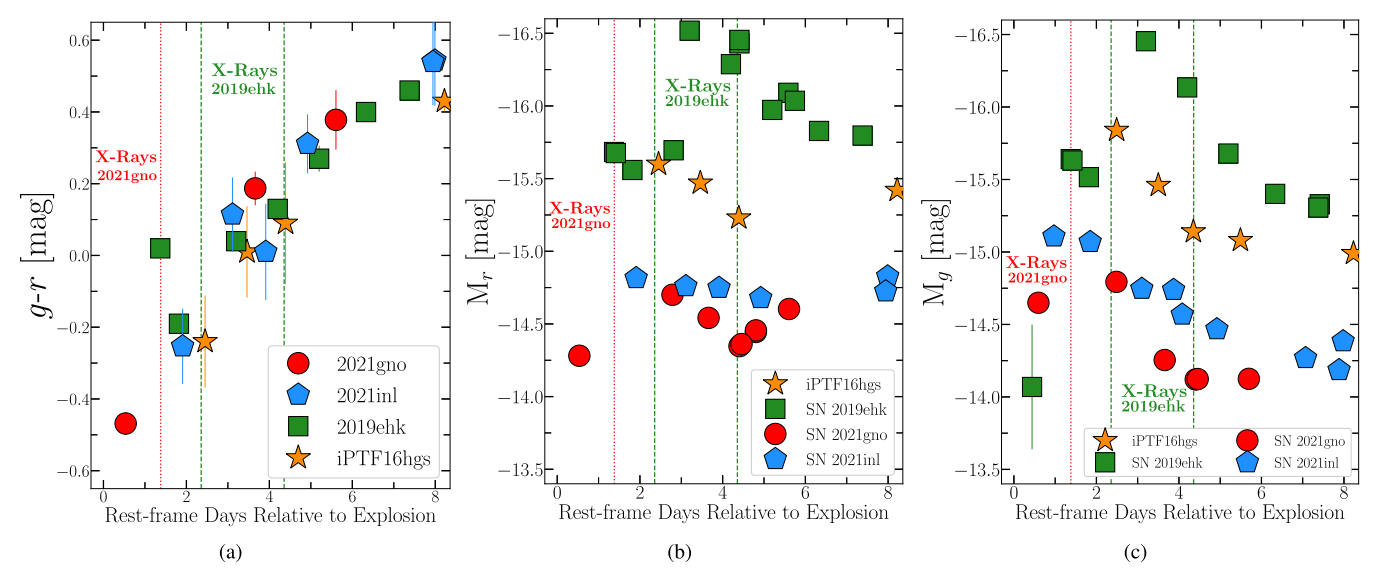


Figure 14. (a) g-r color comparison of SNe 2021gno (red circles), 2021inl (blue polygons), 2019ehk (green squares), and iPTF16hgs (orange stars) during the primary light-curve peak. Phases of X-ray detections in SNe 2021gno and 2019ehk shown as dotted red and dashed green lines, respectively. (b)/(c) Absolute magnitude r-and g-band (left and right) photometry of all four CaSTs during their primary light-curve peak.

10¹³ cm. These CSM properties are based on SCE model parameters (Section 6.2) and X-ray/radio observations (Section 7), and allow us to create a fiducial model for comparisons to observations as well as rough estimations of CSM properties in both objects.

These models are presented with respect to both objects' bolometric luminosities during the early time flux excess in Figure 17. As shown in the plot, both model light curves overestimate the total luminosity in the primary light-curve peak for both SNe; this indicates that the CSM mass is likely lower than that used in the simulations, i.e., $M_{\rm csm} \lesssim 0.02\,M_{\odot}$. For reference, we also plot the CSM interaction model designed for SN 2019ehk's early time excess ($M_{\rm csm} = 1.5 \times 10^{-3}\,M_{\odot}$, $R_{\rm csm} = 10^{14}\,{\rm cm}$), which yields a better match to the light-curve peak in SNe 2021gno and 2021inl. Furthermore, based on these model comparisons, the inferred CSM properties in SN 2021gno are consistent with the CSM mass independently inferred from X-ray modeling in Section 7.

7. CSM Constraints from X-Ray/Radio Emission in SN 2021gno

SN 2021gno is the second CaST, after SN 2019ehk (WJG20a), to show luminous X-ray emission ($L_x \approx 5 \times 10^{41}$ erg s⁻¹) at very early time phases ($\delta t \approx 1$ days), as shown in Figure 5(a). Given the consistency with a rapidly-decaying X-ray emission ($L_x \propto t^{-3}$) and the hard spectrum (Section 2.3), we suggest that, like SN 2019ehk, the X-ray luminosity observed in SN 2021gno is most likely derived from thermal bremsstrahlung emission from shocked CSM gas in an adiabatic expansion. Emission measures are $EM = n^2V$, and we can derive the properties of the local CSM density in SN 2021gno by the following relation:

$$n = [(EM)(\mu_a \mu_I)(4\pi R^2 \Delta R f)^{-1}]^{1/2}$$
(3)

where μ_e , μ_I are the electron and ion molecular weights, respectively, R is the radius of the CSM, ΔR is the CSM thickness, and f is the filling factor (i.e., how homogeneous the

shell of CSM is around the progenitor). For the expression above, we use an emission measure of $EM = (1.8 \pm$ 0.7) $\times 10^{64}$ cm⁻³, filling factor f = 1, and $\mu_e = \mu_I$ assuming H-rich CSM, and the CSM thickness is $\Delta R \approx R$. Because the exact CSM extent is unknown, we calculate multiple possible particle densities based on different CSM geometries. For a shock traveling with speed $v_s = 0.1c$, the location of the blastwave at the time of X-ray emission ($\delta t \approx 1$ day) gives $R_{\rm CSM} = 3 \times 10^{14}$ cm and thus a particle density of $n = (9.4 \pm 1.9) \times 10^9$ cm⁻³. Assuming a H-rich CSM composition, this yields a CSM density of $\rho_{\text{CSM}} = (1.6 \pm 0.3) \times 10^{-14} \text{ g cm}^{-3}$ and mass of $M_{\text{CSM}} = (1.6 \pm 0.3) \times 10^{-3} M_{\odot}$, assuming a spherical geometry. If the CSM radius is in fact comparable to the blackbody radius at $\delta t \approx 1$ day (e.g., $R_{\rm CSM} = 9 \times 10^{13}$ cm), as was done for the X-ray analysis of SN 2019ehk (WJG20a), we find a CSM density and mass of $\rho_{\text{CSM}} = (7.4 \pm 1.5) \times 10^{-14}$ g cm⁻³ and $M_{\rm CSM} = (3.4 \pm 0.7) \times 10^{-4} M_{\odot}$, respectively.

At larger distances from the progenitor, we interpret the radio upper limits discussed in Section 2.4 ($\delta t = 35 - 245$ days) in the context of synchrotron emission from electrons accelerated to relativistic speeds at the explosion's forward shock, as the SN shock expands into the medium. To derive the parameters of the medium, we adopt the synchrotron selfabsorption (SSA) formalism by Chevalier (1998), and we selfconsistently account for free-free absorption (FFA) following Weiler et al. (2002; however, see Terreran et al. 2022; and Jacobson-Galán et al. (2022); for application and additional details on these derivations). For the calculation of the free-free optical depth $\tau_{\rm ff}(\nu)$, we adopt a wind-like density profile $\rho_{\rm csm} \propto r^{-2}$ in front of the shock, and we conservatively assume a gas temperature $T = 10^4 \,\mathrm{K}$ (higher gas temperatures would lead to tighter density constraints). The resulting SSA+FFA synchrotron spectral energy distribution depends on the radius of the emitting region, the magnetic field, the environment density, and the shock microphysical parameters ϵ_B and ϵ_e (i.e., the fraction of post-shock energy density in magnetic fields and relativistic electrons, respectively).

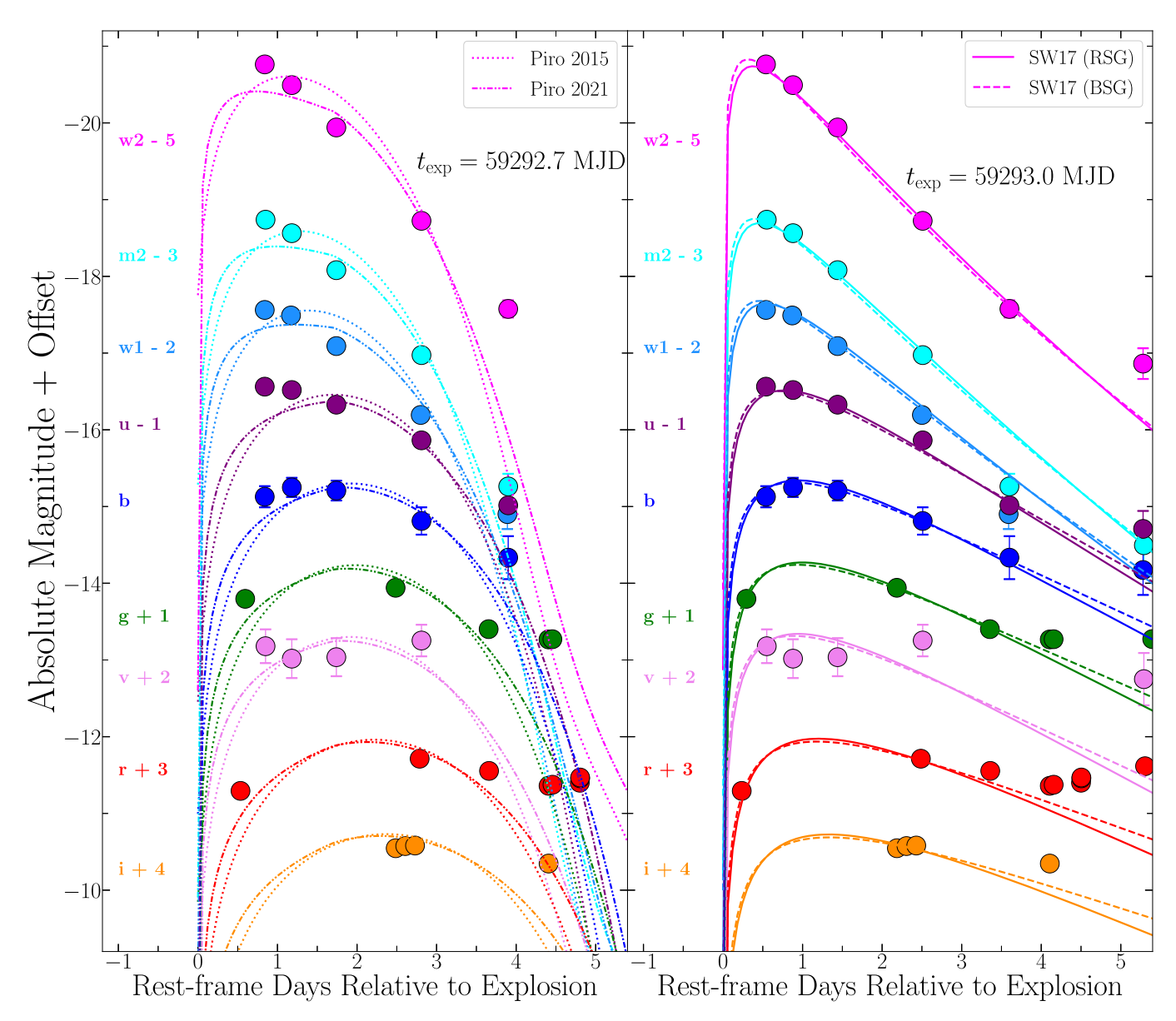


Figure 15. Multicolor shock cooling model fits to the first light-curve peak in SN 2021gno assuming a blackbody SED. Left: Piro (2015) and Piro et al. (2021) models are presented as dotted and dotted—dashed lines, respectively. Right: Sapir & Waxman (2017) models shown as dashed (n = 3) and solid (n = 3/2) lines. Model specifics are discussed in Section 6.2, and physical parameters are presented in Table A6.

At the time of the latest radio nondetection in SN 2021gno, the shock will have probed distances of $r \approx 2 \times 10^{16}$ cm for $v_s = 10^4$ km s⁻¹; however this distance could vary based on the chosen shock speed. We find that, for typical microphysical parameters $\epsilon_B = 0.01$ and $\epsilon_e = 0.1$ (same as for CaST SN 2019ehk; WJG20a), the lack of radio emission indicates a low-density medium that corresponds to a progenitor mass-loss rate of $\dot{M} < 10^{-4} M_{\odot} \text{ yr}^{-1}$, for an adopted wind speed of $v_w = 500 \text{ km s}^{-1}$. This v_w value is the same as in SN 2019ehk, which had direct detections of CSM velocity based on shockionized emission lines in the early time spectra (WJG20a). Overall, the mass-loss limits of both SNe 2021gno and 2019ehk are consistent with one another, the latter being more constraining given the depth of the radio observations.

8. Discussion

8.1. A Physical Progenitor Model

The high-cadence, multiwavelength follow-up of SNe 2021gno and 2021inl allows for some of the best constraints to be made on CaST progenitor systems to date. For SN 2021gno, modeling of the bolometric light curve has revealed that the explosion was low energy ($E_k \approx 1.3 \times 10^{50}$ erg), which produced $\sim 0.6\,M_\odot$ of ejecta and synthesized $\sim 0.012\,M_\odot$ of 56 Ni. Furthermore, the multiband light curve revealed a flux excess above the radioactive-decay-powered continuum emission that lasted ~ 5 days post explosion. Modeling of this primary light-curve peak (e.g., Section 6.2) suggests that the progenitor star could have had an extended

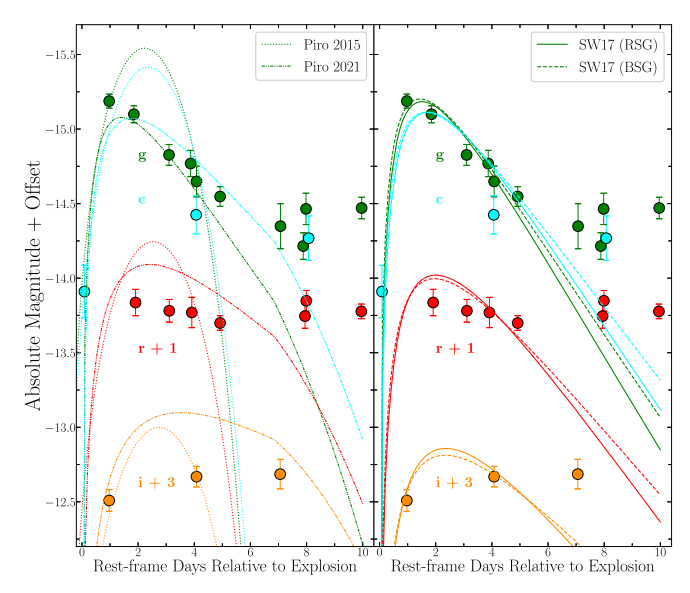


Figure 16. Multicolor shock cooling model fits to the first light-curve peak in SN 2021inl assuming a blackbody SED. *Left:* Piro (2015) and Piro et al. (2021) models are presented as dotted and dotted–dashed lines, respectively. *Right:* Sapir & Waxman (2017) models shown as dashed (n = 3) and solid (n = 3/2) lines. Model specifics are discussed in Section 6.2, and physical parameters are presented in Table A6.

envelope of material with radius $R_e=30-230\,R_\odot$ and mass $M_e=(1.5-4.5)\times 10^{-2}M_\odot$. Additionally, modeling of the luminous X-ray emission detected in SN 2021gno at ~1 day after explosion indicates that the progenitor system also contained a shell of CSM that extended to $R\approx (0.9-3)\times 10^{14}\,\mathrm{cm}$ and was comprised of $\sim (0.3-1.6)\times 10^{-3}M_\odot$ of H-and/or He-rich gas, if the CSM composition is similar to SN 2019ehk. In Figure 17, we show that this amount of CSM can also be the power-source behind the multiband primary light-curve peak; this material being ejected by the progenitor star in the final months before explosion for a possible wind velocity of $\sim 500\,\mathrm{km\,s^{-1}}$. Lastly, the radio nondetections at late-times suggest a relatively clean progenitor environment at distances of $10^{16-17}\,\mathrm{cm}$ and a progenitor mass-loss rate in the final year(s) before explosion of $\dot{M} < 10^{-4}\,M_\odot\,yr^{-1}$.

The above information allows for decent constraints to be made on the potential progenitor star(s) responsible for SN 2021gno. One progenitor scenario is that SN 2021gno resulted from a low-mass, massive star (\sim 8–11 M_{\odot}) that experienced enough enhanced mass loss prior to explosion to remove all stellar H-rich material as well as to place $\sim (1-4) \times 10^{-2} M_{\odot}$ of extended material/envelope at distances $\lesssim 230 R_{\odot}$ and/or $\sim (0.3 - 1.6) \times 10^{-3} M_{\odot}$ CSM at $r \lesssim 3 \times 10^{-3} M_{\odot}$ 10¹⁴ cm. A massive star progenitor is also consistent with the location of SN 2021gno in the spiral arm of a star-forming hostgalaxy. However, the increased mass loss in such a progenitor could only have taken place in the final months before explosion given the low mass-loss rate of $\dot{M} < 10^{-4} M_{\odot} yr^{-1}$ in the year(s). Compared to simulations, progenitor's final SN 2021gno's ejecta mass is consistent with the collapse of a $9-10\,M_{\odot}$ progenitor (Wanajo et al. 2018), but the total synthesized Ni mass is, on average, an order of magnitude lower in these models. Similarly, from BPASS library (Eldridge et al. 2017), all massive star explosions occurring in binary systems in the lowest-mass bins (e.g., $8-11\,M_\odot$) produce $> 1.5\,M_\odot$ of ejecta and synthesize a total ⁵⁶Ni mass that is inconsistent with SN 2021gno. Furthermore, while ultra-stripped SN (USSN)

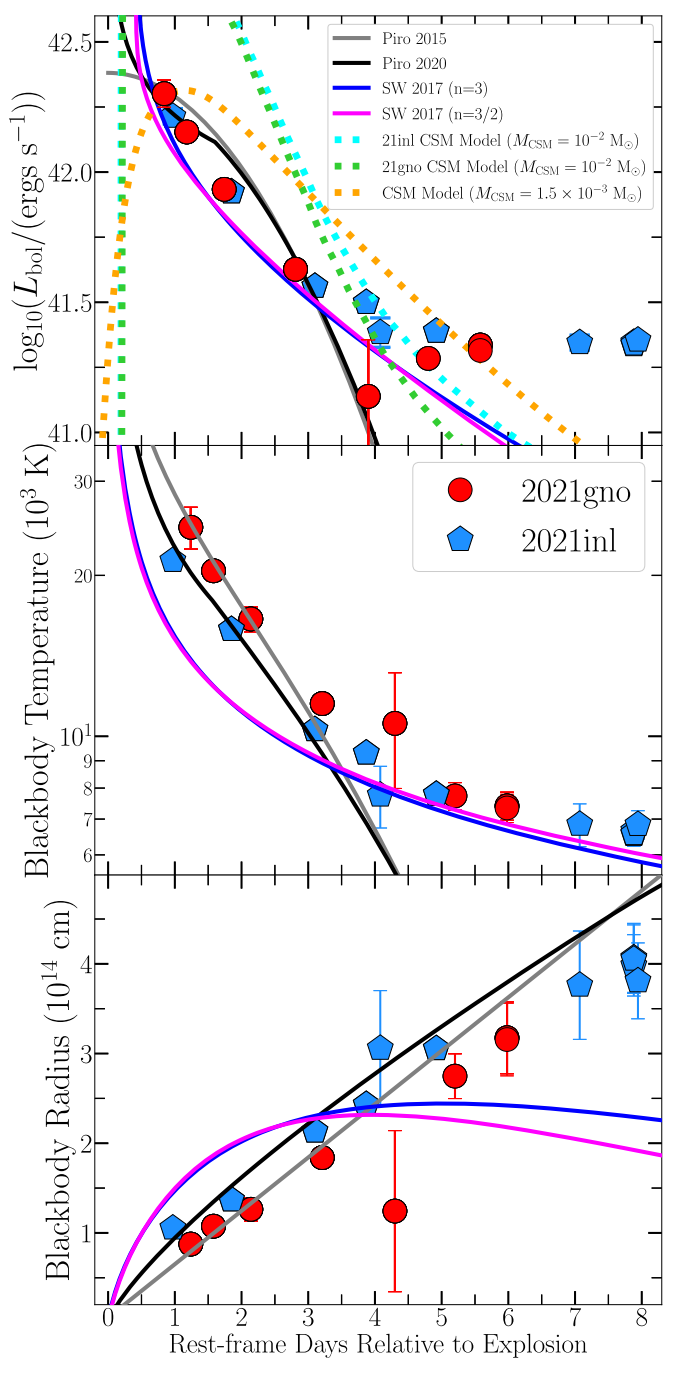


Figure 17. *Top*: bolometric luminosity during the primary light-curve peaks in SNe 2021gno and 2021inl. Shock interaction models plotted as orange/cyan/green dashed lines (see Section 6.3). Shock cooling models are plotted as solid lines: Piro (2015) in gray, Piro et al. (2021) in black, Sapir & Waxman (2017) n=3/2[3] in pink[blue]. SCE model parameters: $M_e=0.02-0.5\,M_\odot$, $R_e=40-230\,R_\odot$, and $v_e=(7-9)\times10^4{\rm km~s^{-1}}$. *Middle*: Blackbody temperatures during the primary light-curve peak. For the interaction model, we show the effective blackbody temperature. *Bottom*: Blackbody radii during the primary light-curve peak. The shock interaction model presents the radius of the emitting region.

progenitor models (e.g., Yoshida et al. 2017; Moriya et al. 2017) produce $M_{\rm ej} \lesssim 0.2\,M_{\odot}$, they can reproduce the Ni yield observed in SN 2021gno, but it is unclear whether these progenitors can retain enough of a He-rich envelope to produce SCE as well as CSM capable of luminous X-ray emission via shock interaction. Lastly, a promising progenitor candidate is a

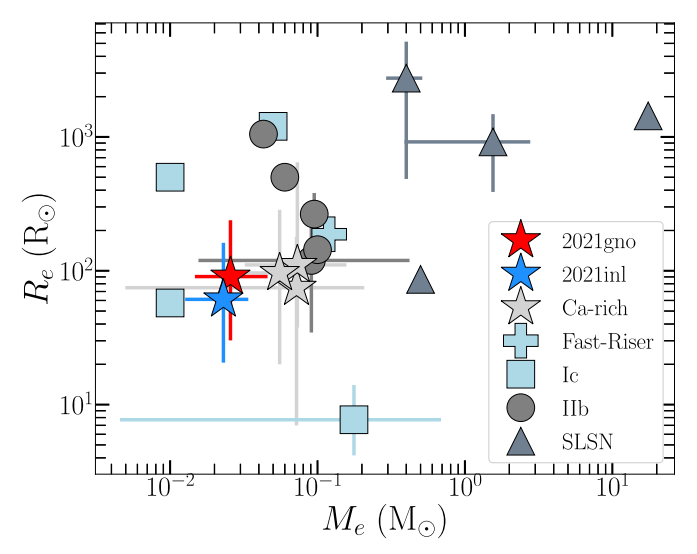


Figure 18. Radius vs. mass of extended material derived from light-curve modeling with shock cooling emission models (e.g., see Section 6.2 for discussion of representative sample). Double-peaked CaSTs shown as stars (2021gno in red, 2021inl in blue), fast-rising transients as blue plus signs, SNe Ic as blue squares, SNe IIb as gray circles, and superluminous SNe as gray triangles. Note that not all of these double-peaked SN light curves were fit with exactly the same SCE models.

He-star binary system capable of producing a type Ib-like explosion (e.g., see Yoon et al. 2017; Jung et al. 2022). Based on the models presented in Table A6 of WJG20a, the ejecta mass of SN 2021gno is consistent with a He-star with an artificial envelope removal (e.g., models #2, 4) and a He-star + NS binary (models #7, 8), both ending in O core burning. However, all of these models would be ruled out if the X-ray emission is derived from H-rich CSM. Furthermore, it is difficult to reconcile a massive star progenitor with the nondetection of a star-forming region at the SN 2021gno explosion site (Section 3) and a SFR of $<3.4\times10^{-5}\,M_\odot\,{\rm yr}^{-1}$, under the assumption of on-going star formation. Given these constraints on a massive star progenitor for SN 2021gno, it may be the case that a WD system is better suited to reproduce the SN observables, as discussed below for SN 2021inl.

In terms of constraining the progenitor of SN 2021inl, the large offset of the SN from an early-type elliptical galaxy makes a massive star progenitor system very unlikely. Consequently, a more plausible scenario is one that involves the explosion of a WD in a binary system. However, such an explosion needs to produce $\sim 0.3\,M_\odot$ of ejecta and $\sim 0.012\,M_\odot$ of 56 Ni, as well as allow for either SCE from a confined ($\sim 20-150\,R_\odot$) and low-mass ($\sim 0.02\,M_\odot$) extended envelope and/or $\lesssim 10^{-3}\,M_\odot$ of CSM. While such a SN is unable to be formed by the typical SN Ia explosion channels, the formation of a confined, extended envelope can occur during the ejection of material in "tidal tails" that then "settles" around the primary WD prior to merger (Raskin & Kasen 2013; Shen et al. 2012; Schwab et al. 2016).

We explore the possibility that SN 2021inl resulted from a double degenerate system containing a hybrid and a CO WD, which was initially presented by WJG20a to explain SN 2019ehk. In this scenario, the tidal disruption of the hybrid HeCO WD by lower-mass CO WD (or another hybrid WD) can induce a He-detonation that can lead to a CaST-like transient (Bobrick et al. 2017; Perets et al. 2019; Zenati et al. 2019b, 2019a). Furthermore, prior to the disruption, significant

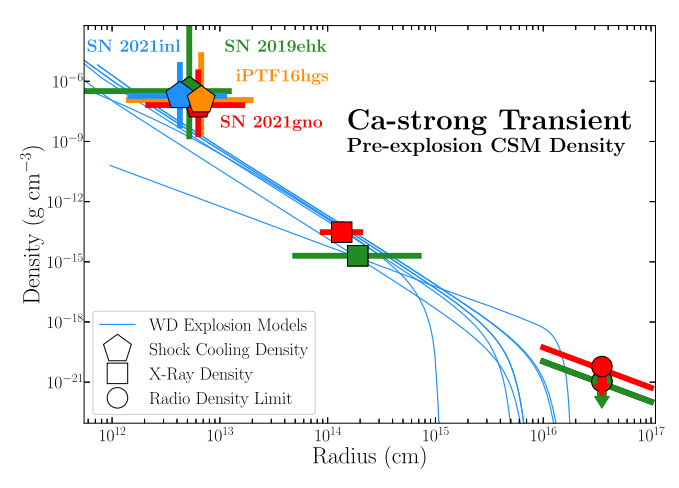


Figure 19. Density profile of the explosion environment of CaSTs 2021gno (red), 2021inl (blue), 2019ehk (green), and iPTF16hgs (orange). Densities plotted as polygons are derived from shock cooling modeling. Shown as red and green squares are density limits derived from X-ray detections in SNe 2021gno and 2019ehk, respectively. The red and green circles are the density limits derived from modeling of the radio nondetections in SNe 2021gno and 2019ehk (WJG20a), respectively. Blue lines are CSM models for WD mergers at the time of explosion (see Section 8.1).

mass transfer ($\dot{M} \approx 10^{-2} \, M_\odot \, yr^{-1}$) will place CSM in the local environment, capable of powering the initial light-curve peak observed in SN 2021inl. We note that such a system could also reproduce the observables in SN 2021gno such as $M_{\rm ej}$ and $M(^{56}{\rm Ni})$ (e.g., see Table A3 of Jacobson-Galán et al. 2021), as well as X-ray emission from CSM interaction and the lack of detectable star formation at the explosion site. In Figure 19, we show the density profiles in the preexplosion environments of SNe 2019ehk, 2021gno, 2021inl, and iPTF16hgs derived from SCE models as well as X-ray and radio modeling for SNe 2019ehk and 2021gno specifically. We show that the preexplosion environments are consistent with the CSM density profiles of WD disruption models discussed above, further indicating that this scenario may be a plausible model to explain these CaSTs.

8.2. SNe 2021 gno and 2021 inl in the Calcium-strong Class

Based on the observational properties of both SNe 2021gno and 2021inl, it is evident that these objects fit within the confines of the CaST observational class. As discussed in Section 4.1, both SNe display low-luminosity ($M_{\rm r,peak}\approx-15$ mag) and rapidly evolving ($t_{\rm r}\approx 8-15$ days) light curves whose color evolutions are consistent with other confirmed CaSTs (e.g., Figure 6). Furthermore, the spectroscopic evolution of SNe 2021gno and 2021inl also solidifies their place in this observational class: both objects show type I spectra near peak, which quickly transitions to an optically thin regime where all nebular emission is dominated by [Ca II] emission and weak [O I] (e.g., [Ca II]/[O I] > 2; Figure 13).

Nonetheless, these SNe do appear to deviate from normative CaST characteristics based on their double-peaked light curves and preexplosion environments. With regards to the former, SNe 2021gno and 2021inl now represent the fourth and fifth confirmed CaSTs with early time flux excesses, the other events being iPTF16hgs, SN 2018lqo, and SN 2019ehk. The observation of this primary light-curve peak confirms the presence of an extended stellar envelope capable of producing SCE and/or a dense CSM that powers the initial flux excess

through SN shock interaction in at least some CaST progenitor systems. Of the 9 CaSTs discovered <3 days after explosion and with <2 day photometric cadence, 5 (55%) show a clear early time flux excess: iPTF16hgs, SNe 2018lqo, 2019ehk, 2021gno, and 2021inl. However, it is possible that 100% of these objects show this signature given the marginal detections of a very early time flux excess in the remaining subsample objects PTF11kmb, PTF12bho, SN 2018kyj, and SN 2019hty, indicating that this feature is potentially ubiquitous to CaSTs.

In terms of their progenitor environments, both SNe exist in visibly different host-galaxies, the large projected offset of SN 2021inl from its early-type host-galaxy being most similar to the environments of many other CaSTs (Perets et al. 2010, 2011; Kasliwal et al. 2012; Lyman et al. 2013, 2014; Perets 2014; Foley 2015; Lunnan et al. 2017; De et al. 2020; Perets & Beniamini 2021). Additionally, despite the fact that SN 2021gno exploded in a star-forming, late-type galaxy, there is no evidence for star formation at the explosion site (similar to SN 2019ehk), which makes this event quite similar to other CaSTs in spite of the visibly different host-galaxy type. However, a number of CaSTs have been discovered in spiral host-galaxies with explosion site star formation (e.g., iPT-F15eqv, iPTF16hgs, SN 2016hnk; Milisavljevic et al. 2017; De et al. 2018a; Galbany et al. 2019), as well as in, or offset from, disk galaxies (e.g., PTF09dav, SN 2001co, SN 2003H, SN 2003dr, SN 2003dg; Sullivan et al. 2011; Kasliwal et al. 2012; Perets 2014; Foley 2015). This spread in CaST host environments continues to indicate that the progenitor systems responsible for these transients are likely heterogeneous, some arising from certain types of massive stars, and others coming from the explosion of compact stars such as WDs.

Lastly, SN 2021gno is now the second confirmed CaST to be detected in X-rays, a novel observational probe for this explosion class. The X-ray emission in SN 2021gno was detected earlier than SN 2019ehk (WJG20a), in addition to being more luminous, but was nonetheless consistent with a rapidly declining rate of $L_x \approx t^{-3}$. Now that this behavior has been confirmed in more than one CaST, it is more likely that X-ray emission from shock interaction in a dense, confined shell of CSM is a trait that could be more common to the CaST class as a whole. However, detecting future CaSTs at X-ray wavelengths requires the discovery of future objects at $D \lesssim 40$ Mpc and the follow-up of these transients with X-ray telescopes in the first \sim day after explosion. Given that X-rays were detected in both SNe 2019ehk and 2021gno, the only two CaSTs where Swift-XRT was repointed at very early phases $(\delta t < 4 \text{ days})$, it is highly likely that X-ray emission is present in all double-peaked, and possibly all single-peaked, CaSTs directly after explosion.

9. Conclusions

In this paper, we have presented multiwavelength observations of two new CaSTs, SNe 2021gno and 2021inl. Despite their unique double-peaked light curves, both objects are photometrically and spectroscopically consistent with prototypical CaSTs throughout their evolution, which solidifies their place in this explosion class. Below we list the primary findings that make SNe 2021gno and 2021inl significant and novel additions to our understanding of these peculiar explosions:

 SN 2021gno was first detected within 0.5 days of explosion and is located on the outer edge of the star-forming spiral

- host-galaxy NGC 4165. SN 2021inl was first detected within 0.1 days of explosion and is located at a large offset from early-type host-galaxy NGC 4923.
- 2. Based on their fast light-curve evolution ($t_r \lesssim 15$ days), low-overall luminosities ($M_{\rm g, peak} > -15$ mag), and dominant [Ca II] emission lines (e.g., [Ca II]/[O I] ≈ 10), both SNe can be confidently classified as CaSTs. Furthermore, the ratio of ion masses derived for both SNe in Section 5.2 (e.g., M(O) > M(Ca)) continues to indicate that these explosions are not "rich" in Ca abundance but rather are "rich" in Ca emission, i.e., "Calcium-strong."
- 3. Despite visibly different host-galaxies, modeling of the host spectra reveals that the explosion sites of both SNe had very little ($\lesssim 10^{-5} M_{\odot} \text{ yr}^{-1}$) or no recent star formation, which strongly suggests that neither SN came from a massive star progenitor.
- 4. SN 2021gno is the second CaST with confirmed, luminous X-ray emission $(L_x \approx 5 \times 10^{41} \text{ erg s}^{-1})$ as detected by Swift-XRT at $\delta t \approx 0.8$ days post explosion. Based on the rapid fading and modeling of the X-ray spectrum, we conclude that this emission was derived from shocked CSM gas comprised of $M_{\text{CSM}} = (0.3-1.6)\times 10^{-3}M_{\odot}$ of shocked gas that extended to distances $R = (0.9-3)\times 10^{14}$ cm, possibly comprised of H- and/or He-rich material. At larger distances from the progenitor star (e.g., $\sim 10^{16-17}$ cm), modeling of SN 2021gno radio observations indicates a progenitor mass-loss rate of $\dot{M} < 10^{-4} M_{\odot} \ yr^{-1} \ (v_w = 500 \ \text{km s}^{-1})$ in the final year(s) before explosion.
- 5. SNe 2021gno and 2021inl are the fourth and fifth CaSTs with multicolor, double-peaked light curves. We model the initial flux excess using four analytic formalisms for shock cooling emission from extended material to derive best-fit parameters of this material (Section 6.2). For SN 2021gno, we find that a radius and mass of the extended material ranging from $R_e \approx 30-230\,R_\odot$ and $M_e \approx 0.02-0.05\,M_\odot$, respectively, can reproduce the early time emission. Similarly, for SN 2021inl, we derive radius and mass of extended material of $R_e \approx 20-150\,R_\odot$ and $M_e \approx 0.02\,M_\odot$, respectively.
- 6. Given the direct evidence for CSM interaction in SN 2021gno, we also model the primary light-curve peak in both SNe with numerical models for shock interaction with confined CSM (Section 6.3). We find that the observed flux excess in SN 2021gno can be fit with $R_{\rm CSM} = 10^{13-14} \, {\rm cm}$ and $M_{\rm CSM} \lesssim 10^{-2} \, M_{\odot}$, both properties being consistent with X-ray modeling. For SN 2021inl, we find a similar best-fit CSM radius and mass.
- 7. Using a combination of shock cooling, shock interaction, X-ray, and radio modeling, as well as host-galaxy SFR, we are able to place some of the tightest constraints to date on the density profile of the local CaST progenitor environment (Figure 19). For both SNe 2021gno and 2021inl, as well as other double-peaked CaSTs SN 2019ehk and iPTF16hgs, the progenitor CSM density is consistent with the models for the merger of low-mass, hybrid WDs. For SNe 2019ehk, 2021gno, and 2021inl specifically, this is supported by the lack of host-galaxy star formation at the explosion sites of these events.

Future multiwavelength (X-ray to radio) observations of double-peaked CaSTs at very early time phases will be instrumental in filling out the progenitor environment phase space and constraining the progenitor channel of these peculiar explosions. Multicolor transient surveys with higher limiting magnitudes (>21 mag) such as YSE currently and LSST in the future will greatly increase the number of CaSTs discovered within a day of explosion.

Research at UC Berkeley is conducted on the territory of Huichin, the ancestral and unceded land of the Chochenyo speaking Ohlone people, the successors of the sovereign Verona Band of Alameda County. Keck I/II, ATLAS, and PS1 observations were conducted on the stolen land of the kānaka 'õiwi people. We stand in solidarity with the Pu'uhonua o Pu'uhuluhulu Maunakea in their effort to preserve these sacred spaces for native Hawai'ians. MMT observations were conducted on the stolen land of the Tohono O'odham and Hia-Ced O'odham nations; the Ak-Chin Indian Community, and Hohokam people. ZTF observations were conducted on the stolen land of the Pauma and Cupeño tribes; the Kumeyaay Nation and the Payómkawichum (Luise no) people. Shane 3-m observations were conducted on the stolen land of the Ohlone (Costanoans), Tamyen, and Muwekma Ohlone tribes.

The Young Supernova Experiment and its research infrastructure is supported by the European Research Council under the European Union's Horizon 2020 research and innovation program (ERC grant agreement No. 101002652, PI K. Mandel), the Heising-Simons Foundation (2018-0913, PI R. Foley; 2018-0911, PI R. Margutti), NASA (NNG17PX03C, PI R. Foley), NSF (AST-1720756, AST-1815935, PI R. Foley; AST-1909796, AST-1944985, PI R. Margutti), the David & Lucille Packard Foundation (PI R. Foley), VILLUM FONDEN (project number 16599, PI J. Hjorth), and the Center for AstroPhysical Surveys (CAPS) at the National Center for Supercomputing Applications (NCSA) and the University of Illinois Urbana-Champaign.

W.J.-G. is supported by the National Science Foundation Graduate Research Fellowship Program under grant No. DGE-1842165. W.J.-G. acknowledges support through NASA grants in support of Hubble Space Telescope program GO-16075 and 16500. This research was supported in part by the National Science Foundation under grant No. NSF PHY-1748958. R.M. acknowledges support by the National Science Foundation under Award No. AST-1909796 and AST-1944985. R.M. is a CIFAR Azrieli Global Scholar in the Gravity & the Extreme Universe Program, 2019. The Margutti's team at Northwestern and UC Berkeley is partially funded by the Heising-Simons Foundation under grant #2018-0911 and #2021-3248 (PI: Margutti).

V.A.V. acknowledges support by the National Science Foundation under Award No.AST-2108676. C.R.A. was supported by grants from VILLUM FONDEN (project numbers 16599 and 25501). Parts of this research were supported by the Australian Research Council Centre of Excellence for All Sky Astrophysics in 3 Dimensions (ASTRO 3D), through project number CE170100013.

The UCSC team is supported in part by NASA grant 80NSSC20K0953, NSF grant AST-1815935, the Gordon & Betty Moore Foundation, the Heising-Simons Foundation, and by a fellowship from the David and Lucile Packard Foundation to R.J.F.

Some of the data presented herein were obtained at the W. M. Keck Observatory, which is operated as a scientific partnership among the California Institute of Technology, the University of California, and NASA. The Observatory was made possible by the generous financial support of the W. M. Keck Foundation. The authors wish to recognize and acknowledge the very significant cultural role and reverence that the summit of Maunakea has always had within the indigenous Hawaiian community. We are most fortunate to have the opportunity to conduct observations from this mountain.

A major upgrade of the Kast spectrograph on the Shane 3 m telescope at Lick Observatory was made possible through generous gifts from the Heising-Simons Foundation as well as William and Marina Kast. Research at Lick Observatory is partially supported by a generous gift from Google.

Based in part on observations obtained with the Samuel Oschin 48 inch Telescope at the Palomar Observatory as part of the Zwicky Transient Facility project, ZTF is supported by the NSF under grant AST-1440341 and a collaboration including Caltech, IPAC, the Weizmann Institute for Science, the Oskar Klein Center at Stockholm University, the University of Maryland, the University of Washington, Deutsches Elektronen-Synchrotron and Humboldt University, Los Alamos National Laboratories, the TANGO Consortium of Taiwan, the University of Wisconsin at Milwaukee, and the Lawrence Berkeley National Laboratory. Operations are conducted by the Caltech Optical Observatories (COO), the Infrared Processing and Analysis Center (IPAC), and the University of Washington (UW).

The Pan-STARRS1 Surveys (PS1) and the PS1 public science archive have been made possible through contributions by the Institute for Astronomy, the University of Hawaii, the Pan-STARRS Project Office, the Max-Planck Society and its participating institutes, the Max Planck Institute for Astronomy, Heidelberg and the Max Planck Institute for Extraterrestrial Physics, Garching, The Johns Hopkins University, Durham University, the University of Edinburgh, the Queen's University Belfast, the Harvard-Smithsonian Center for Astrophysics, the Las Cumbres Observatory Global Telescope Network Incorporated, the National Central University of Taiwan, STScI, NASA under grant NNX08AR22G issued through the Planetary Science Division of the NASA Science Mission Directorate, NSF grant AST-1238877, the University of Maryland, Eotvos Lorand University (ELTE), the Los Alamos National Laboratory, and the Gordon and Betty Moore Foundation. W. M. Keck Observatory and MMT Observatory access was supported by Northwestern University and the Center for Interdisciplinary Exploration and Research in Astrophysics (CIERA).

IRAF is distributed by NOAO, which is operated by AURA, Inc., under cooperative agreement with the National Science Foundation (NSF).

Facilities: Neil Gehrels Swift Observatory, AMI, Zwicky Transient Facility, ATLAS, YSE/PS1, Shane (Kast), MMT (Binospec), Keck I/II (LRIS).

Software: IRAF (Tody 1986, Tody 1993), photpipe (Rest et al. 2005), DoPhot (Schechter et al. 1993), HOTPANTS (Becker 2015), HEAsoft (v6.22; HEASARC 2014), CASA (v6.1.2; McMullin et al. 2007), Sedona (Kasen et al. 2006), Castro (Almgren et al. 2010).

Appendix

In this section we present data Tables A1, A2 and A3 for all X-ray, spectroscopic and radio observations SN 2021gno, respectively. Table A4 presents the spectroscopic observations of SN 2021inl. Table A5 presents the explosion parameters for

CaSTs and Table A6 shows the best fitting shock cooling model parameters for SNe 2021gno and 2021inl. Tables A7 and A8 present photometric observations of SNe 2021inl and 2021gno, respectively.

Table A1 X-Ray Observations of SN 2021gno

MJDs	Phase ^a (days)	Photon Index (Γ)	$0.3-10 \text{ keV Unabsorbed Flux} $ $(10^{-12} \text{ erg s}^{-1} \text{ cm}^{-2})$	Instrument
59293.51, 59293.84	0.81-1.14	$0.74^{+0.50}_{-0.52}$	$4.1^{+2.2}_{-2.1}$	Swift-XRT
59294.36, 59295.44, 59296.23	1.66-3.53		<1.6 ^b	Swift-XRT
59298.28, 59302.66, 59303.14, 59308.71	5.58-16.01		<4.2	Swift-XRT
59313.30, 59317.86, 59325.64, 59414.17, 59524.21	20.6-231.51		<7.3	Swift-XRT

Notes.

Table A2Optical Spectroscopy of SN 2021gno

UT Date	UT Date MJD Phase ^a (days)		Telescope	Instrument	Wavelength Range (Å)
2021-03-22	59295	+2.3	NOT	ALFOSC	3600–9000
2021-03-22	59295	+2.3	Shane	Kast	3300-10200
2021-03-30	59303	+10.3	ANU 2.3 m	WiFES	3800-7000
2021-04-01	59305	+12.4	Livermore Telescope	SPRAT	3800-8000
2021-04-02	59306	+13.3	NOT	ALFOSC	3600-9000
2021-04-06	59310	+17.3	Shane	Kast	3300-10200
2021-04-10	59314	+21.3	IRTF	SpeX	7000-25000
2021-04-13	59317	+24.3	Shane	Kast	3300-10200
2021-04-19	59323	+30.3	Shane	Kast	3300-10200
2021-05-03	59337	+44.3	Shane	Kast	3300-10200
2021-05-12	59346	+53.3	Keck	LRIS	3000-10000
2021-04-09	59376	+83.3	MMT	Binospec	3800–9200

Note.

Table A4Optical Spectroscopy of SN 2021inl

UT Date	MJD	Phase ^a (days)	Telescope	Instrument	Wavelength Range (Å)
2021-04-13	59317	+7.7	Shane	Kast	3300-10200
2021-04-19	59323	+13.7	Shane	Kast	3300-10200
2021-05-12	59346	+36.7	Keck	LRIS	3000-10000
2021-07-08	59403	+93.7	Keck	LRIS	3000-10000

Note.

^a Relative to explosion (MJD 59292.7).

^b Flux calibration performed assuming same spectral parameters inferred at t = +1.21-1.54 d.

^a Relative to explosion (MJD 59292.7).

^a Relative to explosion (MJD 59309.4).

Table A3 VLA Radio Observations of SN 2021gno

Start Date (UT)	Time ^a (days)	Frequency (GHz)	Bandwidth (GHz)	Flux Density ^b (μJy/beam)
2021-04-21	35	15.5	5	€258
2021-04-25	39	15.5	5	€276
2021-11-19	245	15.5	5	€285

Table A5 **Explosion Parameters**

SN	Peak ^a Luminosity (erg s ⁻¹)	$M_{ m ej} \ (M_{\odot})$	E_k (erg)	$M(^{56}\mathrm{Ni})$ (M_{\odot})	(km s^{-1})
2021gno	$(4.12 \pm 1.57) \times 10^{41}$	0.60 ± 0.01	$(1.3 \pm 0.2) \times 10^{50}$	$(1.20 \pm 0.02) \times 10^{-2}$	6000
2021inl	$(2.37 \pm 0.05) \times 10^{41}$	0.60 ± 0.01	$(9.6 \pm 0.4) \times 10^{49}$	$(6.90 \pm 0.06) \times 10^{-3}$	7500
2019ehk ^b	$(9.81 \pm 0.15) \times 10^{41}$	0.72 ± 0.04	$(1.8 \pm 0.1) \times 10^{50}$	$(3.1 \pm 0.11) \times 10^{-2}$	6500
iPTF16hgs ^c	$\sim 3 \times 10^{41}$	0.38	2.3×10^{50}	8.0×10^{-3}	10000
Ca-Ib/c ^d		0.1-0.4		1.5×10^{-2}	$(6-10)\times10^4$

Table A6
Shock Cooling Models

Model	SN	Phase Range days	$R_e \ R_{\odot}$	$[\times 10^{-2}] M_{\odot}$	$[\times 10^3] \mathrm{km \ s^{-1}}$	$t_{ m off}$ Days	χ^2_{ν}
Piro (2015)	2021gno	t < 5	$62.0_{-0.69}^{+0.70}$	$1.72^{+0.015}_{-0.013}$	6.6 ± 0.40	$0.001^{+0.002}_{-0.001}$	105
Piro et al. (2021)	2021gno	<i>t</i> < 5	$231.5_{-8.2}^{+7.8}$	$1.51^{+0.03}_{-0.03}$	$6.19^{+0.06}_{-+0.05}$	$0.01^{+0.001}_{-0.001}$	51.3
Sapir & Waxman (2017) [n=3/2]	2021gno	<i>t</i> < 5	$31.1^{+1.12}_{-1.10}$	$4.47^{0.10}_{-0.010}$	$7.07^{+0.14}_{-0.14}$	$0.28^{+0.010}_{-0.010}$	10.8
Sapir & Waxman (2017) [n=3]	2021gno	<i>t</i> < 5	$37.4^{+1.39}_{-1.25}$	$50.4^{+1.30}_{-1.26}$	$8.57^{+0.19}_{-0.19}$	$0.31^{+0.0091}_{-0.01}$	10.2
Piro (2015)	2021inl	<i>t</i> < 6	$156.8^{+6.93}_{-6.1}$	$2.29^{+0.10}_{-0.10}$	5.2 ± 0.20	$0.01^{+0.002}_{-0.001}$	40.1
Piro et al. (2021)	2021inl	<i>t</i> < 6	$21.2^{+1.71}_{-1.50}$	$37.1^{+24.7}_{-12.6}$	$9.46^{+0.63}_{-0.67}$	$0.003^{+0.004}_{-0.002}$	7.91
Sapir & Waxman (2017) [n=3/2]	2021inl	<i>t</i> < 6	$24.7^{+5.34}_{-4.03}$	$18.7^{+4.20}_{-3.50}$	$5.26^{+0.23}_{-0.23}$	$0.003^{+0.003}_{-0.002}$	5.57
Sapir & Waxman (2017) [n=3]	2021inl	<i>t</i> < 6	$42.7_{-4.83}^{+7.13}$	$170^{+19.5}_{-27.3}$	$5.15_{-0.25}^{+0.23}$	$0.004^{+0.004}_{-0.002}$	3.71

Notes. ^a Relative to explosion (MJD 59292.7). ^b Upper limits are quoted at 3σ .

Notes.

a Second, radioactive-decay-powered light-curve peak.
b Jacobson-Galán et al. (2020a).
c De et al. (2018a).
d De et al. (2020).

Table A7 Optical Photometry of SN 2021inl

Table A8 Optical Photometry of SN 2021gno

							<u> </u>				
MJD	Phase ^a	Filter	Magnitude	Uncertainty	Instrument	MJD	Phase ^a	Filter	Magnitude	Uncertainty	Instrument
59310.36	+0.97	g	19.51	0.05	PS1	59293.29	+0.59	g	17.74	0.02	ZTF
59312.49	+3.10	g	19.87	0.07	PS1	59296.35	+3.65	g	18.13	0.03	ZTF
59313.47	+4.08	g	20.05	0.10	PS1	59298.39	+5.69	g	18.26	0.06	ZTF
59314.31	+4.92	g	20.15	0.07	PS1	59302.35	+9.65	g	17.64	0.04	ZTF
59316.46	+7.07	g	20.34	0.15	PS1	59304.26	+11.56	g	17.57	0.03	ZTF
59317.37	+7.98	g	20.23	0.10	PS1	59307.31	+14.61	g	17.55	0.01	ZTF
59319.35	+9.96	g	20.22	0.07	PS1	59309.31	+16.61	g	17.80	0.02	ZTF
59321.45	+12.06	g	20.42	0.08	PS1	59311.23	+18.53	g	18.10	0.02	ZTF
59322.49	+13.10	g	20.56	0.11	PS1	59313.26	+20.56	g	18.48	0.03	ZTF
59323.36	+13.97	g	20.71	0.17	PS1	59315.28	+22.58	g	18.64	0.10	ZTF
59350.26	+40.87	g	21.47	0.43	PS1	59321.25	+28.55	g	19.43	0.05	ZTF
59353.37	+43.98	g	22.12	0.63	PS1	59323.28	+30.58	g	19.47	0.08	ZTF
59312.50	+3.11	r	19.75	0.08	PS1	59325.32	+32.62	g	19.48	0.11	ZTF
59314.31	+4.92	r	19.84	0.05	PS1	59335.25	+42.55	g	19.91	0.12	ZTF
59317.38	+7.99	r	19.69	0.07	PS1	59338.31	+45.61	g	20.10	0.11	ZTF
59319.34	+9.95	r	19.76	0.05	PS1	59340.21	+47.51	g g	19.98	0.08	ZTF
59321.46	+12.07	r	19.81	0.04	PS1	59342.23	+49.53		20.18	0.09	ZTF
59326.30	+16.91	r	20.21	0.14	PS1	59344.26	+51.56	g	20.32	0.05	ZTF
59332.44	+23.05	r	20.64	0.22	PS1	59350.21	+57.51	g	20.46	0.11	ZTF
59334.43	+25.04	r	21.09	0.55	PS1	59353.23	+60.53	g	20.40	0.10	ZTF
59334.44	+25.04	r	20.92	0.33	PS1	59362.18	+69.48	g	20.02	0.31	ZTF
59336.44	+27.05	r	21.08	0.20	PS1		+09.48 +72.49	g	20.93	0.19	ZTF
59344.27	+34.88	r	21.47	0.24	PS1	59365.19		g			
59352.43	+43.04		21.50	0.17	PS1	59367.25	+74.55	g	20.88	0.23	ZTF
59360.27	+43.04 +50.88	r r	22.04	0.55	PS1	59369.23	+76.53	g	20.91	0.20	ZTF
				0.09	PS1	59371.19	+78.49	g	21.28	0.29	ZTF
59364.40	+55.01	r	22.28			59373.18	+80.48	g	21.07	0.22	ZTF
59375.37	+65.98	r	22.52	0.88	PS1	59376.22	+83.52	g	20.96	0.31	ZTF
59414.28	+104.89	<i>r</i>	22.37	0.87	PS1	59378.19	+85.49	g	21.18	0.31	ZTF
59310.36	+0.97	i	20.02	0.07	PS1	59293.24	+0.54	r	18.20	0.03	ZTF
59313.47	+4.08	i	19.86	0.07	PS1	59296.36	+3.66	r	17.94	0.03	ZTF
59316.45	+7.06	i	19.84	0.10	PS1	59298.30	+5.60	r	17.88	0.06	ZTF
59322.49	+13.10	i	19.77	0.05	PS1	59302.26	+9.56	r	17.33	0.03	ZTF
59323.35	+13.96	i	19.72	0.06	PS1	59304.30	+11.60	r	17.16	0.02	ZTF
59326.30	+16.91	i	19.66	0.10	PS1	59307.25	+14.55	r	17.05	0.01	ZTF
59334.42	+25.03	i	20.71	0.51	PS1	59309.27	+16.57	r	17.08	0.01	ZTF
59342.27	+32.88	i	20.91	0.18	PS1	59311.31	+18.61	r	17.22	0.01	ZTF
59346.40	+37.01	i	21.25	0.21	PS1	59313.30	+20.60	r	17.39	0.02	ZTF
59349.45	+40.06	i	21.56	0.51	PS1	59315.25	+22.55	r	17.53	0.22	ZTF
59351.38	+41.99	i	20.82	0.26	PS1	59317.21	+24.51	r	17.83	0.02	ZTF
59362.39	+53.00	i	21.82	0.50	PS1	59321.29	+28.59	r	18.08	0.02	ZTF
59368.34	+58.95	i	21.98	0.54	PS1	59323.32	+30.62	r	18.23	0.03	ZTF
59373.33	+63.94	i	22.25	0.33	PS1	59325.26	+32.56	r	18.32	0.03	ZTF
59332.44	+23.05	z	20.85	0.34	PS1	59335.21	+42.51	r	18.72	0.05	ZTF
59334.44	+25.05	z	21.10	0.33	PS1	59338.23	+45.53	r	18.90	0.04	ZTF
59336.44	+27.05	Z	20.56	0.28	PS1	59340.23	+47.53	r	19.08	0.05	ZTF
59353.37	+43.98	z	21.01	0.31	PS1	59342.28	+49.58	r	19.15	0.05	ZTF
59360.26	+50.87	z	21.40	0.47	PS1	59344.23	+51.53	r	19.18	0.04	ZTF
59364.41	+55.02	z	21.40	0.31	PS1	59346.31	+53.61	r	19.34	0.07	ZTF
59366.41	+57.02	z	21.55	0.38	PS1	59348.19	+55.49	r	19.33	0.05	ZTF
59414.28	+104.89	z	21.79	0.66	PS1	-					

(This table is available in its entirety in machine-readable form.)

(This table is available in its entirety in machine-readable form.)

Note. ^a Relative to explosion (MJD 59309.4).

^a Relative to explosion (MJD 59292.7).

ORCID iDs

W. V. Jacobson-Galán https://orcid.org/0000-0002-P. Venkatraman https://orcid.org/0000-0001-8638-2780 R. Margutti https://orcid.org/0000-0003-4768-7586 D. Khatami https://orcid.org/0000-0003-4307-0589 G. Terreran https://orcid.org/0000-0003-0794-5982 R. J. Foley https://orcid.org/0000-0002-2445-5275 C. R. Angus https://orcid.org/0000-0002-4269-7999 K. Auchettl https://orcid.org/0000-0002-4449-9152 P. K. Blanchard https://orcid.org/0000-0003-0526-2248 A. Bobrick https://orcid.org/0000-0002-4674-0704 J. S. Bright https://orcid.org/0000-0002-7735-5796 D. Brout https://orcid.org/0000-0001-5201-8374 K. C. Chambers https://orcid.org/0000-0001-6965-7789 D. A. Coulter https://orcid.org/0000-0003-4263-2228 T. J. L. de Boer https://orcid.org/0000-0001-5486-2747 L. DeMarchi https://orcid.org/0000-0003-4587-2366 S. A. Dodd https://orcid.org/0000-0002-3696-8035 D. O. Jones https://orcid.org/0000-0002-6230-0151 C. D. Kilpatrick https://orcid.org/0000-0002-5740-7747 N. Khetan https://orcid.org/0000-0003-2720-8904 D. Langeroodi https://orcid.org/0000-0001-5710-8395 C.-C. Lin https://orcid.org/0000-0002-7272-5129 E. A. Magnier https://orcid.org/0000-0002-7965-2815 D. Milisavljevic https://orcid.org/0000-0002-0763-3885 H. B. Perets https://orcid.org/0000-0002-5004-199X J. D. R. Pierel https://orcid.org/0000-0002-2361-7201 J. Raymond https://orcid.org/0000-0002-7868-1622 S. Rest https://orcid.org/0000-0002-3825-0553 A. Rest https://orcid.org/0000-0002-4410-5387 R. Ridden-Harper https://orcid.org/0000-0003-1724-2885 K. J. Shen https://orcid.org/0000-0002-9632-6106 M. R. Siebert https://orcid.org/0000-0003-2445-3891 K. Taggart https://orcid.org/0000-0002-5748-4558 S. Tinyanont https://orcid.org/0000-0002-1481-4676 F. Valdes https://orcid.org/0000-0001-5567-1301 V. A. Villar https://orcid.org/0000-0002-5814-4061 Q. Wang https://orcid.org/0000-0001-5233-6989 S. K. Yadavalli https://orcid.org/0000-0002-0840-6940 Y. Zenati https://orcid.org/0000-0002-0632-8897 A. Zenteno https://orcid.org/0000-0001-6455-9135

References

```
Albareti, F. D., Allende Prieto, C., Almeida, A., et al. 2017, ApJS, 233, 25
Almgren, A. S., Beckner, V. E., Bell, J. B., et al. 2010, ApJ, 715, 1221
Arcavi, I., Gal-Yam, A., Yaron, O., et al. 2011, ApJL, 742, L18
Arcavi, I., Hosseinzadeh, G., Brown, P. J., et al. 2017, ApJL, 837, L2
Armstrong, P., Tucker, B. E., Rest, A., et al. 2021, MNRAS, 507, 3125
Arnett, W. D. 1982, ApJ, 253, 785
Becker, A. 2015, HOTPANTS: High Order Transform of PSF ANd Template
   Subtraction, Astrophysics Source Code Library, ascl:1504.004
Bellm, E. C., Kulkarni, S. R., Graham, M. J., et al. 2019, PASP, 131, 018002
Bobrick, A., Davies, M. B., & Church, R. P. 2017, MNRAS, 467, 3556
Brown, P. J., Breeveld, A. A., Holland, S., Kuin, P., & Pritchard, T. 2014,
   Ap&SS, 354, 89
Brown, P. J., Roming, P. W. A., Milne, P., et al. 2010, ApJ, 721, 1608
Bruch, R., Zimmerman, E., & Johansson, J. 2021, Transient Name Server
  Discovery Report, 202-8431
Bruzual, G., & Charlot, S. 2003, MNRAS, 344, 1000
Burrows, D. N., Hill, J. E., Nousek, J. A., et al. 2005, SSRv, 120, 165
Cappellaro, E., Mazzali, P. A., Benetti, S., et al. 1997, A&A, 328, 203
Chabrier, G. 2003, in IAU Symp. 221, Star Formation at High Angular
```

Resolution (Cambridge: Cambridge Univ. Press), P67

```
Chambers, K. C., Huber, M. E., Flewelling, H., et al. 2017, Transient Name
  Server Discovery Report, 207-3241
Chevalier, R. A. 1998, ApJ, 499, 810
Conroy, C., Gunn, J. E., & White, M. 2009, ApJ, 699, 486
De, K., Fremling, U. C., Gal-Yam, A., et al. 2021, ApJL, 907, L18
De, K., Kasliwal, M. M., Cantwell, T., et al. 2018a, ApJ, 866, 72
De, K., Kasliwal, M. M., Ofek, E. O., et al. 2018b, Sci, 362, 201
De, K., Kasliwal, M. M., Tzanidakis, A., et al. 2020a, ApJ, 905, 58
Dong, Y., Milisavljevic, D., Leja, J., et al. 2022, ApJ, 927, 199
Duffell, P. C. 2016, RT1D: 1D code for Rayleigh-Taylor instability,
  Astrophysics Source Code Library, ascl:1607.015
Eldridge, J. J., Stanway, E. R., Xiao, L., et al. 2017, PASA, 34, e058
Filippenko, A. V., Chornock, R., Swift, B., et al. 2003, IAU Circ., 8159, 2
Fitzpatrick, E. L. 1999, PASP, 111, 63
Foley, R. J. 2015, MNRAS, 452, 2463
Foley, R. J., Papenkova, M. S., Swift, B. J., et al. 2003, PASP, 115, 1220
Foreman-Mackey, D., Hogg, D. W., Lang, D., & Goodman, J. 2013, PASP,
Gagliano, A., Izzo, L., Kilpatrick, C. D., et al. 2022, ApJ, 924, 55
Galbany, L., Anderson, J. P., Sánchez, S. F., et al. 2018, ApJ, 855, 107
Galbany, L., Ashall, C., Hoeflich, P., et al. 2019, A&A, 630, A76
Gehrels, N., Chincarini, G., Giommi, P., et al. 2004, ApJ, 611, 1005
Graham, M. J., Kulkarni, S. R., Bellm, E. C., et al. 2019, PASP, 131, 078001
Hickish, J., Razavi-Ghods, N., Perrott, Y. C., et al. 2018, MNRAS, 475, 5677
Ho, A. Y. Q., Kulkarni, S. R., Perley, D. A., et al. 2020, ApJ, 902, 86
Horne, K. 1986, PASP, 98, 609
Hung, T., Tinyanont, S., Dimitriadis, G., & Foley, R. J. 2021, Transient Name
  Server Classification Report, 202-8841
Jacobson-Galán, W. V., Margutti, R., Kilpatrick, C. D., et al. 2020a, ApJ,
  898, 166
Jacobson-Galán, W. V., Polin, A., Foley, R. J., et al. 2020b, ApJ, 896, 165
Jacobson-Galán, W. V., Margutti, R., Kilpatrick, C. D., et al. 2021, ApJL,
  908, L32
Jacobson-Galán, W. V., Dessart, L., Jones, D. O., et al. 2022, ApJ, 924, 15
Jarrett, T. H., Chester, T., Cutri, R., et al. 2000, AJ, 119, 2498
Jones, D. O., Foley, R. J., Narayan, G., et al. 2021, ApJ, 908, 143
Jung, M.-K., Yoon, S.-C., & Kim, H.-J. 2022, ApJ, 925, 216
Kaiser, N., Aussel, H., Burke, B. E., et al. 2002, Proc. SPIE, 4836, 154
Kalberla, P. M. W., Burton, W. B., Hartmann, D., et al. 2005, A&A, 440, 775
Kasen, D., Thomas, R. C., & Nugent, P. 2006, ApJ, 651, 366
Kasliwal, M. M., Kulkarni, S. R., Gal-Yam, A., et al. 2012, ApJ, 755, 161
Kennicutt, R. C. J. 1998, ARA&A, 36, 189
Kouveliotou, C., Woosley, S. E., Patel, S. K., et al. 2004, ApJ, 608, 872
Kriek, M., van Dokkum, P. G., Labbé, I., et al. 2009, ApJ, 700, 221
Kuncarayakti, H., Anderson, J. P., Galbany, L., et al. 2018, A&A, 613, A35
Lunnan, R., Kasliwal, M. M., Cao, Y., et al. 2017, ApJ, 836, 60
Lyman, J. D., James, P. A., Perets, H. B., et al. 2013, MNRAS, 434, 527
Lyman, J. D., Levan, A. J., Church, R. P., Davies, M. B., & Tanvir, N. R. 2014,
  MNRAS, 444, 2157
Margutti, R., Zaninoni, E., Bernardini, M. G., et al. 2013, MNRAS, 428,
  729
Masci, F. J., Laher, R. R., Rusholme, B., et al. 2019, PASP, 131, 018003
McMullin, J. P., Waters, B., Schiebel, D., Young, W., & Golap, K. 2007, in
   ASP Conf. Ser., 376, Astronomical Data Analysis Software and Systems
  XVI, ed. R. A. Shaw, F. Hill, & D. J. Bell (San Francisco, CA: ASP), 127
Milisavljevic, D., Patnaude, D. J., Raymond, J. C., et al. 2017, ApJ, 846, 50
Miller, J. S., & Stone, R. P. S. 1993, LOTRM, https://mthamilton.ucolick.org/
  techdocs/instruments/kast/Tech%20Report%2066%20KAST%20Miller%
   20Stone.pdf
Moriya, T. J., Mazzali, P. A., Tominaga, N., et al. 2017, MNRAS, 466, 2085
Munoz-Arancibia, A., Forster, F., Bauer, F. E., et al. 2021, Transient Name
   Server Discovery Report, 202-10921
Nakaoka, T., Maeda, K., Yamanaka, M., et al. 2021, ApJ, 912, 30
Nakar, E., & Piro, A. L. 2014, ApJ, 788, 193
Oke, J. B., Cohen, J. G., Carr, M., et al. 1995, PASP, 107, 375
Perets, H. B. 2014, arXiv:1407.2254
Perets, H. B., Badenes, C., Arcavi, I., Simon, J. D., & Gal-yam, A. 2011, ApJ,
  730.89
Perets, H. B., & Beniamini, P. 2021, MNRAS, 503, 5997
Perets, H. B., Zenati, Y., Toonen, S., & Bobrick, A. 2019, arXiv:1910.07532
Perets, H. B., Gal-Yam, A., Mazzali, P. A., et al. 2010, Natur, 465, 322
Perrott, Y. C., Scaife, A. M. M., Green, D. A., et al. 2013, MNRAS, 429, 3330
Pettini, M., & Pagel, B. E. J. 2004, MNRAS, 348, L59
Piro, A. L. 2015, ApJL, 808, L51
Piro, A. L., Haynie, A., & Yao, Y. 2021, ApJ, 909, 209
Piro, A. L., Muhleisen, M., Arcavi, I., et al. 2017, ApJ, 846, 94
```

```
Raskin, C., & Kasen, D. 2013, ApJ, 772, 1
Rest, A., Stubbs, C., Becker, A. C., et al. 2005, ApJ, 634, 1103
Rest, A., Dhawan, S., Mandel, K., et al. 2022, TNSAN, 24, 1
Roming, P. W. A., Kennedy, T. E., Mason, K. O., et al. 2005, SSRv, 120, 95
Roth, N., & Kasen, D. 2015, ApJS, 217, 9
Salpeter, E. E. 1955, ApJ, 121, 161
Sapir, N., & Waxman, E. 2017, ApJ, 838, 130
Schechter, P. L., Mateo, M., & Saha, A. 1993, PASP, 105, 1342
Schlafly, E. F., & Finkbeiner, D. P. 2011, ApJ, 737, 103
Schlegel, D. J., Finkbeiner, D. P., & Davis, M. 1998, ApJ, 500, 525
Schwab, J., Quataert, E., & Kasen, D. 2016, MNRAS, 463, 3461
Seibert, M., Wyder, T., Neill, J., et al. 2012, AAS Meeting, 219, 340.01
Shen, K. J., Bildsten, L., Kasen, D., & Quataert, E. 2012, ApJ, 748, 35
Shen, K. J., Quataert, E., & Pakmor, R. 2019, ApJ, 887, 180
Silverman, J. M., Foley, R. J., Filippenko, A. V., et al. 2012, MNRAS,
   425, 1789
Smith, K. W., Smartt, S. J., Young, D. R., et al. 2020, PASP, 132, 085002
Smith, M., Sullivan, M., D'Andrea, C. B., et al. 2016, ApJL, 818, L8
Sullivan, M., Kasliwal, M. M., Nugent, P. E., et al. 2011, ApJ, 732, 118
Sutherland, P. G., & Wheeler, J. C. 1984, ApJ, 280, 282
Taggart, K., Rojas-Bravo, C., Foley, R. J., & Angus, C. R. 2021, Transient
  Name Server Classification Report, 202-11961
```

```
Taubenberger, S. 2017, in The Extremes of Thermonuclear Supernovae, ed.
  A. Alsabti & P. Murdin, Vol. 317 (Cham: Springer)
Terreran, G., Jacobson-Galan, W. V., Groh, J. H., et al. 2022, ApJ, 926, 20
Theureau, G., Hanski, M. O., Coudreau, N., Hallet, N., & Martin, J. M. 2007,
  A&A 465 71
Tonry, J. L., Denneau, L., Heinze, A. N., et al. 2018a, PASP, 130, 064505
Tonry, J. L., Denneau, L., Flewelling, H., et al. 2018b, ApJ, 867, 105
Valenti, S., Benetti, S., Cappellaro, E., et al. 2008, MNRAS, 383, 1485
Wade, R. A., & Horne, K. 1988, ApJ, 324, 411
Wanajo, S., Müller, B., Janka, H.-T., & Heger, A. 2018, ApJ, 852, 40
Weiler, K. W., Panagia, N., Montes, M. J., & Sramek, R. A. 2002, ARA&A,
  40, 387
Wheeler, J. C., Johnson, V., & Clocchiatti, A. 2015, MNRAS, 450, 1295
Wheeler, J. C., Barker, E., Benjamin, R., et al. 1993, ApJL, 417, L71
Yao, Y., De, K., Kasliwal, M. M., et al. 2020, ApJ, 900, 46
Yoon, S.-C., Dessart, L., & Clocchiatti, A. 2017, ApJ, 840, 10
Yoshida, T., Suwa, Y., Umeda, H., Shibata, M., & Takahashi, K. 2017,
         S, 471, 4275
Zenati, Y., Perets, H. B., & Toonen, S. 2019a, MNRAS, 486, 1805
Zenati, Y., Toonen, S., & Perets, H. B. 2019b, MNRAS, 482, 1135
Zwart, J. T. L., Barker, R. W., Biddulph, P., et al. 2008, MNRAS, 391,
```